

Mechanics of Advanced Materials and Structures



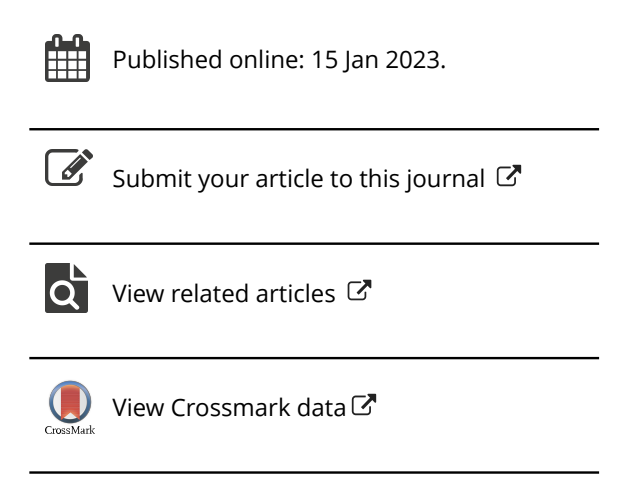
ISSN: (Print) (Online) Journal homepage: https://www.tandfonline.com/loi/umcm20

Optimal local truncation error method for solution of 2-D elastodynamics problems with irregular interfaces and unfitted Cartesian meshes as well as for post-processing

A. Idesman & M. Mobin

To cite this article: A. Idesman & M. Mobin (2023): Optimal local truncation error method for solution of 2-D elastodynamics problems with irregular interfaces and unfitted Cartesian meshes as well as for post-processing, Mechanics of Advanced Materials and Structures, DOI: 10.1080/15376494.2022.2162639

To link to this article: https://doi.org/10.1080/15376494.2022.2162639





ORIGINAL ARTICLE



Optimal local truncation error method for solution of 2-D elastodynamics problems with irregular interfaces and unfitted Cartesian meshes as well as for post-processing

A. Idesman and M. Mobin

Department of Mechanical Engineering, Texas Tech University, Lubbock, TX, USA

ABSTRACT

The optimal local truncation error method (OLTEM) with unfitted Cartesian meshes recently developed for the scalar wave and heat equations for heterogeneous materials is extended to a more complex case of a system of the elastodynamics PDEs. Compact 9-point stencils (similar to those for linear finite elements) are used for OLTEM. Compared to our previous results, a new approach is used for the calculation of the right-hand side of the stencil equations due to body forces. It significantly simplifies the analytical derivations of OLTEM for time-dependent problems. There are no unknowns on interfaces between different materials; the structure of the global semi-discrete equations for OLTEM is the same for homogeneous and heterogeneous materials. For the first time we have also developed OLTEM with the diagonal mass matrix. In contrast to many known approaches with some ad-hoc calculations of the diagonal mass matrix, OLTEM offers a rigorous approach which is a particular case of OLTEM with the non-diagonal mass matrix.

Another novelty of the article is a new post-processing procedure for the accurate calculations of stresses. It includes the same compact 9-point stencils as those in basic computations and uses the accelerations and the displacements at the grid points along with the PDEs for the stress calculations.

OLTEM yields accurate numerical results for heterogeneous materials with big contrasts in the material properties of different components. Numerical experiments for elastic heterogeneous materials show: a) at the same number of degrees of freedom (dof), OLTEM with unfitted Cartesian meshes is more accurate than linear finite elements with similar stencils and conformed meshes; at the engineering accuracy of 0.1% for the displacements, OLTEM reduces the number of dof by more than 20 times; at the engineering accuracy of 0.1% for the stresses, OLTEM with the new post-processing procedure reduces the number of dof by more than 10⁴ times compared to linear finite elements; b) at the same number of dof, OLTEM with unfitted Cartesian meshes is even more computationally efficient than high-order finite elements with much wider stencils and conformed meshes. This will lead to a huge reduction in the computation time for elastodynamics problems solved by OLTEM and will allow the direct computations of some complex wave propagation and structural dynamics problems for heterogeneous materials without the scale separation.

ARTICLE HISTORY

Received 16 June 2022 Accepted 21 December 2022

KEYWORDS

Elastodynamics equations for heterogeneous materials: irregular interfaces; local truncation error; unfitted Cartesian meshes; optimal accuracy

1. Introduction

There are many important engineering problems described by the time-dependent elasticity equations. Accurate numerical solutions of elastodynamics (structural dynamics and wave propagation) problems on complex irregular geometry are time consuming and this restricts the application of numerical methods to many important applications. Therefore, the development of computationally efficient numerical methods for elastodynamics is still a challenging task and many different numerical techniques has been suggested in the recent years (e.g., see [1–9] and many others).

The finite element method, the finite volume method, the isogeometric elements, the spectral elements and similar techniques represent very powerful tools for the solution of partial differential equations (PDEs) for a complex geometry. However, the generation of non-uniform meshes for a complex geometry is not simple and may lead to a significant decrease in accuracy of these techniques for elastodynamics problems if "bad" elements (e.g., elements with small angles) appear in the mesh. There is a significant number of publications related to the numerical solution of different PDEs on irregular domains with uniform embedded meshes. For example, we can mention the following fictitious domain numerical methods that use uniform embedded meshes: the embedded finite difference method, the cut finite element method, the finite cell method, the Cartesian grid method, the immersed interface method, the virtual boundary method, the embedded boundary method, etc.; e.g., see [10-38] and many others. The main objective of these techniques

is to simplify the mesh generation for irregular domains as well as to mitigate the effect of "bad" elements. For example, the techniques based on the finite element formulations (such as the cut finite element method, the finite cell method, the virtual boundary method and others) yield the p+1 order of accuracy even with small cut cells generated due to complex irregular boundaries (e.g., see [11-14, 18, 37] and many others). The main advantage of the embedded boundary method developed in [19-21, 32, 34] is the use of simple Cartesian meshes. The boundary conditions or fluxes in this technique are interpolated using the Cartesian grid points and this leads to the increase in the stencil width for the grid points located close to the boundary (the numerical techniques developed in [19-21, 33, 34] provide the second order of accuracy for the global solution). The development of different numerical techniques (finite difference method, immersed finite element method, immersed meshfree method) for statics elasticity interface problems with unfitted meshes were recently reported in [39-41].

Recently in our papers [42-50] OLTEM has been developed for the solution of PDEs with constant coefficients on regular and irregular domains with Cartesian meshes. At the same structure of the semidiscrete or discrete equations, the new technique provides the optimal order of accuracy of discrete equations that exceeds the order of accuracy of many known numerical approaches on regular and irregular domains. For example, in our paper [46] it was shown that OLTEM with 9-point and 25-point stencils (similar to those for linear and quadratic finite elements) provides the second and sixth orders of accuracy for the 2-D elastodynamics equations on regular domains. The second and sixth orders of accuracy are the optimal accuracy for all elastodynamics numerical techniques with 9-point and 25-point stencils independent of the approach used for their derivations. In our paper [51] we have developed OLTEM with 9-point stencils and unfitted Cartesian meshes to a much more general case of the 2-D time-dependent scalar heat and wave equations with discontinuous coefficients and irregular interfaces and we have obtained the third order of accuracy of the new approach.

Here, OLTEM with unfitted Cartesian meshes recently developed in [51] for the scalar wave and heat equations for heterogeneous materials is extended to a more complex case of a system of the elastodynamics PDEs. Compact 9-point stencils (similar to those for linear finite elements) are used for OLTEM. Compared to our previous results, a new approach is used for the calculation of the right-hand side of the stencil equations due to body forces. It significantly simplifies the analytical derivations of OLTEM for timedependent problems. For the first time we have also developed OLTEM with the diagonal mass matrix. In contrast to many known approaches with some ad-hoc calculations of the diagonal mass matrix (e.g., see [5, 6, 8] and many others), OLTEM offers a rigorous approach which is a particular case of OLTEM with the non-diagonal mass matrix. Another novelty of the article is a new post-processing procedure for the accurate calculations of stresses. In contrast to known finite element post-processing procedures (e.g.,

see [52–54] and others), it includes the same compact 9-point stencils as those in basic computations and uses the accelerations and the displacements at the grid points along with the PDEs for the stress calculations.

The idea of OLTEM for the solution of elastodynamics PDEs is very simple. First, an unfitted Cartesian mesh is selected independent of the irregular domain under consideration. Then, stencil equations of a semi-discrete system are assumed for all internal grid points of the Cartesian mesh located inside the domain. The stencil equation for each internal grid point is a linear combination of the numerical values of the unknown displacements and accelerations at a number of grid points included into the stencil; e.g., see Eq. (6). The stencil equations for all internal grid points form the global semi-discrete system of equations for OLTEM. The coefficients of the stencil equations are assumed to be unknown. These unknown coefficients are determined by the minimization of the order of the local truncation error of the stencil equation. The local truncation error of the stencil equation is obtained by the replacement of an unknown numerical solution for the displacements and accelerations in the stencil equation by an unknown exact solution. According to the new approach suggested in this article, the second order time derivatives in the local truncation error are excluded with the help of the elastodynamics PDEs. Then, substituting a Taylor series expansion of the unknown exact solution at the grid points into the stencil equation, we obtain the local truncation error of the stencil equation in the form of a Taylor series. The unknown coefficients of each stencil equation are calculated from a small local system of algebraic equations. This local system is obtained by equating to zero the lowest terms in the Taylor series expansion of the local truncation error as well as by the minimization of the non-zero leading terms of the local truncation error with the least square method. The coefficients of the stencil equations are similarly calculated for homogeneous (no interfaces) and heterogeneous (with interfaces) stencils. The local truncation error for the heterogeneous stencils additionally includes the known interface conditions at a small number of selected interface points located on the irregular interface. The semi-discrete system of equation does not include unknowns at the interface points. Finally, a semi-discrete global system with unknowns at the internal grid points can be easily integrated by known time-integration methods. The structure of this semi-system is the same for homogeneous and heterogeneous materials (the difference is in the values of the stencil coefficients). The main advantages of OLTEM are an optimal accuracy and the simplicity of the formation of a semi-discrete system for irregular interfaces with unfitted Cartesian meshes. Changing the width of the stencil equations, different linear and high-order numerical techniques can be developed. We should mention that similar to the finite-difference techniques, OLTEM does not use any weak formulation for the derivation of the semi-discrete equations. However, in contrast to the finite-difference techniques with the stencil coefficients calculated through the approximation of separate partial derivatives, the entire system of the elastodynamics

partial differential equations is used for the calculation of the stencil coefficients in OLTEM. This leads to the optimal accuracy of the proposed technique.

The focus of this article is the development of 2-D compact 9-point stencils (similar to those for linear elements) for the elastodynamics equations affected by irregular interfaces between different elastic materials on unfitted Cartesian meshes. These stencils will be used for the calculation of the displacements in basic computations as well as for the stress calculation during post-processing.

The 2-D elastodynamics equations in a composite domain $\Omega = \bigcup \Omega_l$ $(l = 1, 2, ..., \bar{N}$ where \bar{N} is the total number of subdomains) can be written down in each subdomain Ω_l as follows:

$$\mu_{l}\nabla^{2}u_{l} + (\mu_{l} + \lambda_{l})\left(\frac{\partial^{2}u_{l}}{\partial x^{2}} + \frac{\partial^{2}v_{l}}{\partial x\partial y}\right) + f_{x}^{l} = \rho_{l}\frac{\partial^{2}u_{l}}{\partial t^{2}},$$

$$\mu_{l}\nabla^{2}v_{l} + (\mu_{l} + \lambda_{l})\left(\frac{\partial^{2}v_{l}}{\partial y^{2}} + \frac{\partial^{2}u_{l}}{\partial x\partial y}\right) + f_{y}^{l} = \rho_{l}\frac{\partial^{2}v_{l}}{\partial t^{2}},$$
(1)

where $u_l = u_l(x, y, t)$ and $v_l = v_l(x, y, t)$ are the x- and ycomponents of the displacement vector, $f_x^l = f_x^l(x, y, t)$ and $f_{\nu}^{l} = f_{\nu}^{l}(x, y, t)$ are the x- and y- components of the body forces that can be discontinuous across interfaces, t is the time, μ_l and λ_l are Lame coefficients that can be also expressed in terms of Young's modulus E_l and Poisson's ratio ν_l as follows:

$$\mu_l = \frac{E_l}{2(1+\nu_l)}, \qquad \lambda_l = \frac{E_l\nu_l}{(1+\nu_l)(1-2\nu_l)}.$$
(2)

We also assume that the functions u_l and f_l are sufficiently smooth in each subdomain Ω_l . At the interface G between any two subdomains, the following interface conditions (the continuity of the displacements and the tractive forces across the interface) are applied:

$$u_G^* - u_G^{**} = 0, \qquad v_G^* - v_G^{**} = 0,$$
 (3)

$$t_{x,G}^* - t_{x,G}^{**} = 0, t_{y,G}^* - t_{y,G}^{**} = 0,$$
 (4)

where the symbols * and ** correspond to the quantities on the opposite sides from the interface for the corresponding subdomains Ω_l . The x- and y- components of the tractive forces $t_{x,G}$ and $t_{y,G}$ can be expressed in terms of the displacements as follows:

$$t_{x,G} = n_x \left[(\lambda + 2\mu) \frac{\partial u}{\partial x} + \lambda \frac{\partial v}{\partial y} \right] + n_y \mu \left(\frac{\partial u}{\partial y} + \frac{\partial v}{\partial x} \right),$$

$$t_{y,G} = n_y \left[(\lambda + 2\mu) \frac{\partial v}{\partial y} + \lambda \frac{\partial u}{\partial x} \right] + n_x \mu \left(\frac{\partial u}{\partial y} + \frac{\partial v}{\partial x} \right),$$
(5)

where n_x and n_y are the x- and y-components of the unit normal vector at the interface. According to Eqs. (3)–(5), the displacements u and v are continuous across the interfaces but they can have the discontinuous spatial derivatives across the interfaces.

Remark 1. The derivation of the new approach can be easily extended to the case with the discontinuous displacements and tractive forces across interfaces; i.e., when the righthand sides in Eqs. (3) and (4) are the given functions. However, for simplicity we consider Eqs. (3) and (4) with zero right-hand sides.

In this article, the Dirichlet boundary conditions $u = g_1$ and $v = g_2$ are applied along the external boundary Γ where g_1 and g_2 are the given functions. However, the Neumann boundary conditions (tractive forces) can be also used with the proposed approach; e.g., see our papers [47, 55]. According to OLTEM, the semi-discrete system for the elastodynamics equations, Eq. (1), after the space discretization with a Cartesian rectangular mesh can be represented as a system of linear ordinary differential equations (ODEs). The ODEs of this system for each internal grid point of the domain are called the stencil equations. For the 2-D elastodynamics equations, two stencil equations can be written down for each grid point as follows:

$$h^{2}\left(\sum_{i=1}^{L} m_{j,i} \frac{d^{2} u_{i}^{num}}{dt^{2}} + \sum_{i=1}^{L} \bar{m}_{j,i} \frac{d^{2} v_{i}^{num}}{dt^{2}}\right) + \sum_{i=1}^{L} k_{j,i} u_{i}^{num} + \sum_{i=1}^{L} \bar{k}_{j,i} v_{i}^{num} = \bar{f}_{j}, \quad j = 1, 2,$$

$$(6)$$

where u_i^{num} and v_i^{num} as well as $\frac{d^2 u_i^{num}}{dt^2}$ and $\frac{d^2 v_i^{num}}{dt^2}$ are the numerical solution for the displacements u and v as well as for their second order time derivatives at the i-th grid point, $m_{j,i}$, $\bar{m}_{j,i}$, $k_{j,i}$ and $k_{j,i}$ are the unknown stencil coefficients (they should be determined) corresponding to the displacements u and v and their second order time derivatives, L is the number of the grid points included into the stencil, f_i are the components of the discretized body forces (see the next Sections). We should mention that we do not consider the time discretization for the derivation the stencil coefficients $m_{j,i}$, $\bar{m}_{j,i}$, $k_{j,i}$ and $k_{j,i}$ used in OLTEM. These stencil coefficients are related to the space discretization. The time discretization with any known time integration method can be used for the integration of the global system of the semidiscrete equations of OLTEM. Many numerical techniques such as the finite difference method, the finite element method, the finite volume method, the isogeometric elements, the spectral elements, different meshless methods and others can be finally reduced to Eq. (6) with some specific coefficients $m_{j,i}$, $\bar{m}_{j,i}$, $k_{j,i}$ and $k_{j,i}$. In order to demonstrate a new technique, below we will assume compact 9point stencils (L=9) in the 2-D case that correspond to the width of the stencils for linear quadrilateral finite elements on Cartesian meshes and that require similar computational costs as those for linear finite elements. However, the stencils with any width can be used with the suggested approach.

Let us introduce the local truncation error used with OLTEM. The replacement of the numerical values of the displacements u_i^{num} and v_i^{num} at the grid points in Eq. (6) by the exact solution u_i and v_i to the elastodynamics equations, Eq. (1), leads to the residual of these equations called the local truncation error e_i of the semi-discrete equations, Eq. (6):

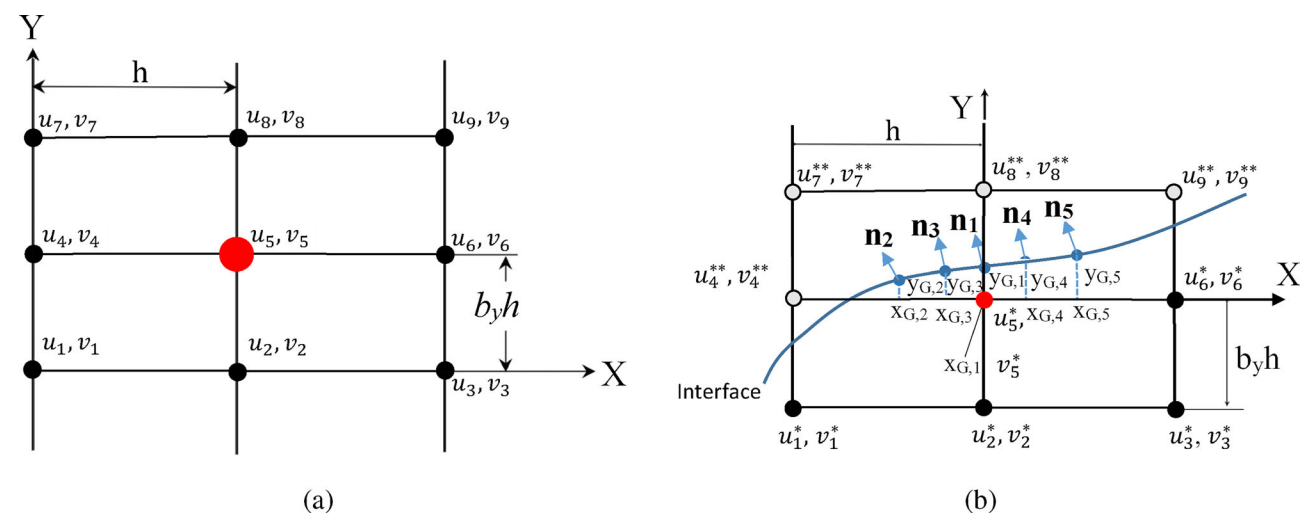


Figure 1. The spatial locations of the degrees of freedom u_p and v_p (p = 1, 2, ..., 9) that contribute to the 9-point uniform stencil for the internal degrees of freedom u_5 and v_5 for homogeneous material without interface (a) and for heterogeneous material with interface (b).

$$e_{j} = h^{2} \left(\sum_{i=1}^{L} m_{j,i} \frac{d^{2} u_{i}}{dt^{2}} + \sum_{i=1}^{L} \bar{m}_{j,i} \frac{d^{2} v_{i}}{dt^{2}} \right) + \sum_{i=1}^{L} k_{j,i} u_{i}$$

$$+ \sum_{i=1}^{L} \bar{k}_{j,i} v_{i} - \bar{f}_{j}, \qquad j = 1, 2.$$

$$(7)$$

Calculating the difference between Eqs. (7) and (6) we can get

$$e_{j} = h^{2} \sum_{i=1}^{L} \left\{ m_{j,i} \left[\frac{d^{2}u_{i}}{dt^{2}} - \frac{d^{2}u_{i}^{num}}{dt^{2}} \right] + \bar{m}_{j,i} \left[\frac{d^{2}v_{i}}{dt^{2}} - \frac{d^{2}v_{i}^{num}}{dt^{2}} \right] \right\}$$

$$+ \sum_{i=1}^{L} \left\{ k_{j,i} \left[u_{i} - u_{i}^{num} \right] + \bar{k}_{j,i} \left[v_{i} - u_{i}^{num} \right] \right\}$$

$$= h^{2} \sum_{i=1}^{L} \left(m_{j,i} \overline{\bar{e}}_{i} + \bar{m}_{j,i} \overline{\bar{e}}_{i}^{*} \right) + \sum_{i=1}^{L} \left(k_{j,i} \overline{e}_{i} + \bar{k}_{j,i} \overline{e}_{i}^{*} \right), \quad j = 1, 2,$$

$$(8)$$

where $\bar{e}_i = u_i - u_i^{num}$, $\bar{e}_i^* = v_i - v_i^{num}$, $\bar{\bar{e}}_i = \frac{d^2 u_i}{dt^2} - \frac{d^2 u_i^{num}}{dt^2}$ and $\bar{\bar{e}}_i^* = \frac{d^2 v_i}{dt^2} - \frac{d^2 v_i^{num}}{dt^2}$ are the errors in the numerical solution for the displacements u, v and their second order time derivatives at the grid point i. As can be seen from Eq. (8), the local truncation errors e_j (j = 1, 2) are a linear combination of the errors in the numerical solution for the displacements u and v and for their second order time derivatives at the grid points which are included into the stencil equations.

In Section 2, OLTEM with 9-point compact stencils and unfitted Cartesian meshes is derived for the calculation of the displacements for the 2-D elastodynamics equations with discontinuous coefficients and irregular interfaces. It includes the derivation of the local truncation error for homogeneous and heterogeneous materials, the derivation of the right-hand side of the stencil equation due to the body forces, the derivation of a small local system of algebraic equations for the calculation of the stencil coefficients as well as the use of the non-diagonal and diagonal mass matrices. Section 3 describes a new post-processing procedure for the stress calculations that includes the same

compact 9-point stencils as those in basic computations and uses the accelerations and the displacements at the grid points along with the PDEs for the stress calculations. Numerical experiments showing the advantages of OLTEM are presented in Section 4. For the derivation of many analytical expressions presented below we use the computational program "Mathematica."

2. OLTEM for the 2-D elastodynamics equations with discontinuous material properties

2.1. 9-Point stencil equations and the corresponding local truncation error

Let us consider a 2-D bounded domain and a Cartesian rectangular mesh with a mesh size h where h is the size of the mesh along the x- axis, $b_y h$ is the size of the mesh along the y- axis (b_y is the aspect ratio of the mesh). To simplify derivations, below we consider regular rectangular domains with irregular interfaces between different materials. However, irregular domains can be also considered with OLTEM; see [42-44]. Here we will develop 9-point uniform stencils that provide the optimal second order of accuracy. We should mention that the same structure of stencils for homogeneous and heterogeneous materials is used (the difference between homogeneous and heterogeneous materials is in the values of the stencil coefficients only). The spatial locations of the 8 grid points that are close to the central grid point with the coordinates x_5 , y_5 and contribute to the 9-point stencil for this central grid point are shown in Figure 1. For convenience, the local numeration of the grid points from 1 to 9 is used in Figure 1 as well as in the derivations below. The interface in Figure 1b divides the 9-point uniform stencil into two parts with different material properties. In order to impose the interface conditions at the interface, we select a small number of interface points as follows. First we select one point at the interface with the coordinates $x_{G,1}$ and $y_{G,1}$. This point can be selected as the shortest distance from the central grid point of the 9-point stencil to the interface. Then, we additionally select n

interface points to the left and to the right from the point with the coordinates $x_{G,1}$ and $y_{G,1}$ at the same distances h= $\sqrt{\left(x_{G,i+1}-x_{G,i}\right)^{2}+\left(y_{G,i+1}-y_{G,i}\right)^{2}}$ (i=1,2,...,2n) from each other; e.g., see Figure 1b for 9-point stencils. The numerical experiments show that small distances $\bar{h} = h/5$ yield accurate results. The total number of selected interface points is $N_G = h/5$ 2n + 1 where $N_G = 5$ is used for the 9-point stencils developed below.

Let us describe the coordinates of the grid points of the 9-point uniform stencils (see Figure 1) with respect to their central point (x_5, y_5) as follows:

$$x_p = x_5 + r_{x,p}h = x_5 + (i-2)h, y_p = y_5 + r_{y,p}b_yh = y_5 + (j-2)b_yh,$$
 (9)

where the coefficients $r_{x,p}$, $r_{y,p}$ are:

$$r_{x,p} = (i-2), r_{y,p} = (j-2),$$
 (10)

and p = 3(j-1) + i with i, j = 1, 2, 3.

To describe the coordinates of the N_G points on the interface (see Figure 1b) we introduce $2N_G$ coefficients $d_{x,p}$ and $d_{y,p}$ $(p = 1, 2, ..., N_G)$ as follows (see also Figure 1b):

$$x_{G,m} = x_5 + d_{x,m}h, y_{G,m} = y_5 + d_{y,m}b_yh, m = 1, 2, ..., N_G.$$
 (11)

Remark 2. Some interface points G_m ($m = 1, 2, ..., N_G$) can be located slightly outside the 9-point cell. The derivations presented below are also valid for these cases.

The stencil equations, Eq. (6), for heterogeneous materials with the 9-point uniform stencil for the grid point (x_5, y_5) (see Figure 1) will be assumed in the following form:

$$h^{2} \left\{ \sum_{p=1}^{9} m_{j,p} \left[a_{p} \frac{d^{2} u_{p}^{*,num}}{dt^{2}} + (1 - a_{p}) \frac{d^{2} u_{p}^{**,num}}{dt^{2}} \right] + \sum_{p=1}^{9} \bar{m}_{j,p} \left[a_{p} \frac{d^{2} v_{p}^{*,num}}{dt^{2}} + (1 - a_{p}) \frac{d^{2} v_{p}^{**,num}}{dt^{2}} \right] \right\}$$

$$+ \sum_{p=1}^{9} k_{j,p} \left[a_{p} u_{p}^{*,num} + (1 - a_{p}) u_{p}^{**,num} \right] + \sum_{p=1}^{9} \bar{k}_{j,p} \left[a_{p} v_{p}^{*,num} + (1 - a_{p}) v_{p}^{**,num} \right] = \bar{f}_{j,5}, \qquad j = 1, 2,$$

$$(12)$$

where $\bar{f}_{j,5} = 0$ in the case of zero body forces $f_x^l = f_y^l = 0$ in Eq. (1), the unknown coefficients $m_{j,p}$, $\bar{m}_{j,p}$, $k_{j,p}$ and $\bar{k}_{j,p}$ (p=1,2,...,9) are to be determined from the minimization of the local truncation error, $k_{1,5}=1$, $\bar{k}_{1,5}=0$ for j=1 and $k_{2,5} = 0$, $\bar{k}_{2,5} = 1$ for j = 2 (in this case the stencil coefficients for the two stencils with j = 1 and j = 2 are linearly independent; see also Remark 3 below), the coefficients $a_p = 1$ if the grid point u_p belongs to material * or $a_p = 0$ if the grid point u_p belongs to another material * (i.e., only two variables $u_p^{*,num}$, $v_p^{*,num}$ or $u_p^{**,num}$, $v_p^{**,num}$ are included into Eq. (12) for each grid point; e.g., see Figure 1b with $a_1 = a_2 = a_3 = a_5 = a_6 = 1$ and $a_4 = a_7 = a_8 = a_9 = 0$).

Remark 3. Only 35 out of the 36 coefficients $m_{j,p}$, $\bar{m}_{j,p}$, $k_{j,p}$, $\bar{k}_{j,p}$ (p=1,2,...,9) in Eq. (12) for each stencil can be considered as unknown coefficients. This can be explained as follows. In the case of zero body forces $\bar{f}_{i,5} = 0$, Eq. (12) can be rescaled by the division of the left- and right-hand sides of Eq. (12) by any scalar; i.e., one of the coefficients can be selected as unity and there will be only 35 unknown rescaled coefficients. The case of nonzero body forces $\bar{f}_{i,5} \neq 0$ can be similarly treated because the term $\bar{f}_{i,5}$ is a linear function of the stencil coefficients; see below. For convenience, we will scale the stencil coefficients in such a way that $k_{1,5}$ is $k_{1,5} = 1$ for the first stencil. Moreover, similar to the finite element stencils we select $\bar{k}_{1,5} = 0$.

Remark 4. Usually, stencil equations similar to Eq. (12) include the coefficient h^2 in the denominator in order to express the second space derivatives in the elastodynamics equations, Eq. (1). However, for convenience, the stencil equations, Eq. (12), are multiplied by h^2 in order to write down them without $\frac{1}{h^2}$. Therefore, the expressions for the local truncation error used in the article are also multiplied by h^2 .

The local truncation error e follows from Eq. (12) by the replacement of the numerical solution $u_b^{*,num}$, $u_b^{**,num}$, $v_b^{*,num}$ and $v_p^{**,num}$ by the exact solution u_p^* , u_p^{**} , v_p^* and v_p^{**} :

$$e_{j} = h^{2} \left\{ \sum_{p=1}^{9} m_{j,p} \left[a_{p} \frac{\partial^{2} u_{p}^{*}}{\partial t^{2}} + (1 - a_{p}) \frac{\partial^{2} u_{p}^{**}}{\partial t^{2}} \right] + \sum_{p=1}^{9} \bar{m}_{j,p} \left[a_{p} \frac{\partial^{2} v_{p}^{*}}{\partial t^{2}} + (1 - a_{p}) \frac{\partial^{2} v_{p}^{**}}{\partial t^{2}} \right] \right\}$$

$$+ \sum_{p=1}^{9} k_{j,p} \left[a_{p} u_{p}^{*} + (1 - a_{p}) u_{p}^{**} \right] + \sum_{p=1}^{9} \bar{k}_{j,p} \left[a_{p} v_{p}^{*} + (1 - a_{p}) v_{p}^{**} \right] - \bar{f}_{j,5}, \qquad j = 1, 2.$$

$$(13)$$

One of the ideas of the new approach is to include the interface conditions for the exact solution at a small number of the interface points into Eq. (13) for the local truncation error as follows:

$$e_{j} = h^{2} \left\{ \sum_{p=1}^{9} m_{j,p} \left[a_{p} \frac{\partial^{2} u_{p}^{*}}{\partial t^{2}} + (1 - a_{p}) \frac{\partial^{2} u_{p}^{**}}{\partial t^{2}} \right] + \sum_{p=1}^{9} \bar{m}_{j,p} \left[a_{p} \frac{\partial^{2} v_{p}^{*}}{\partial t^{2}} + (1 - a_{p}) \frac{\partial^{2} v_{p}^{**}}{\partial t^{2}} \right] \right\}$$

$$+ \sum_{p=1}^{9} k_{j,p} \left[a_{p} u_{p}^{*} + (1 - a_{p}) u_{p}^{**} \right] + \sum_{p=1}^{9} \bar{k}_{j,p} \left[a_{p} v_{p}^{*} + (1 - a_{p}) v_{p}^{**} \right]$$

$$+ \left[\sum_{m=1}^{N_{G}} q_{1,m} (u_{G,m}^{*} - u_{G,m}^{**}) + \sum_{m=1}^{N_{G}} q_{2,m} (v_{G,m}^{*} - v_{G,m}^{**}) + \sum_{m=1}^{N_{G}} h q_{3,m} (t_{x(G,m)}^{*} - t_{x(G,m)}^{**}) + \sum_{m=1}^{N_{G}} h q_{4,m} (t_{y(G,m)}^{*} - t_{y(G,m)}^{**}) \right]$$

$$- \bar{f}_{i,5}, \qquad j = 1, 2,$$

$$(14)$$

with

$$t_{x(G,m)}^{*} = n_{x,m} \left[(\lambda_{*} + 2\mu_{*}) \frac{\partial u_{G,m}^{*}}{\partial x} + \lambda_{*} \frac{\partial v_{G,m}^{*}}{\partial y} \right] + n_{y,m} \mu_{*} \left(\frac{\partial u_{G,m}^{*}}{\partial y} + \frac{\partial v_{G,m}^{*}}{\partial x} \right),$$

$$t_{x(G,m)}^{**} = n_{x,m} \left[(\lambda_{**} + 2\mu_{**}) \frac{\partial u_{G,m}^{**}}{\partial x} + \lambda_{**} \frac{\partial v_{G,m}^{**}}{\partial y} \right] + n_{y,m} \mu_{**} \left(\frac{\partial u_{G,m}^{*}}{\partial y} + \frac{\partial v_{G,m}^{**}}{\partial x} \right),$$

$$t_{y(G,m)}^{*} = n_{y,m} \left[(\lambda_{*} + 2\mu_{*}) \frac{\partial v_{G,m}^{*}}{\partial y} + \lambda_{*} \frac{\partial u_{G,m}^{*}}{\partial x} \right] + n_{x,m} \mu_{*} \left(\frac{\partial u_{G,m}^{*}}{\partial y} + \frac{\partial v_{G,m}^{*}}{\partial x} \right),$$

$$t_{y(G,m)}^{**} = n_{y,m} \left[(\lambda_{**} + 2\mu_{**}) \frac{\partial v_{G,m}^{**}}{\partial y} + \lambda_{**} \frac{\partial u_{G,m}^{**}}{\partial x} \right] + n_{x,m} \mu_{**} \left(\frac{\partial u_{G,m}^{**}}{\partial y} + \frac{\partial v_{G,m}^{**}}{\partial x} \right),$$

$$(15)$$

where the expressions in parenthesis after $q_{1,m}$, $q_{2,m}$, $q_{3,m}$ and $q_{4,m}$ in the end of Eq. (14) are the interface conditions at the selected N_G interface points and are equal to zero (see Eqs. 3–5), the coefficients $q_{1,m}$, $q_{2,m}$, $q_{3,m}$ and $q_{4,m}$ ($m=1,2,...,N_G$) will be used for the minimization of the local truncation error in Eq. (14) (these coefficients can be also considered as Lagrange multipliers for the interface conditions), $n_{x,m}$ and $n_{y,m}$ in Eq. (15) are the x- and y-components of the unit normal vectors at the selected N_G interface points (e.g., see Figure 1b). Due to the interface conditions (Eqs. 3 and 4), the expressions in Eqs. (13) and (14) yield the same local truncation error e_j . The addition of the interface conditions at $N_G=5$ points in Eq. (14) with the coefficients $q_{1,m}$, $q_{2,m}$, $q_{3,m}$ and $q_{4,m}$ ($m=1,2,...,N_G$) allows us to get the second order of accuracy of OLTEM for general geometry of interfaces; see below.

Remark 5. In Eq. (14) we consider two local truncation errors for the first j = 1 and second j = 2 stencils. The coefficients $q_{1,m}$, $q_{2,m}$, $q_{3,m}$ and $q_{4,m}$ ($m = 1, 2, ..., N_G$) are different for these two stencils. However, in order to simplify the notations we omit index j for the coefficients $q_{1,m}$, $q_{2,m}$, $q_{3,m}$ and $q_{4,m}$.

2.2. The modification of the local truncation error using the elastodynamics equations as well as the calculation of the loading term $\bar{f}_{i,5}$

Here we show that using the elastodynamics equations, Eq. (1), we can exclude the second order time derivatives $\frac{\partial^2 u_p^*}{\partial t^2}$, $\frac{\partial^2 u_p^*}{\partial t^2}$, $\frac{\partial^2 u_p^*}{\partial t^2}$, $\frac{\partial^2 v_p^*}{\partial t^2}$, $\frac{\partial^2 v_p^*}{\partial t^2}$, $\frac{\partial^2 v_p^*}{\partial t^2}$ in the expression for the local truncation error in Eq. (14) as well as we can define the loading term $\bar{f}_{i,5}$. According to Eq. (1), for the exact solution at the grid points and at the interface points we can write down:

$$\frac{\partial^2 u^*}{\partial t^2} = \bar{u}^* + \frac{1}{\rho^*} f_x^* \qquad \text{with} \qquad \bar{u}^* = \frac{\mu^*}{\rho^*} \nabla^2 u^* + \frac{(\mu^* + \lambda^*)}{\rho^*} \left(\frac{\partial^2 u^*}{\partial x^2} + \frac{\partial^2 v^*}{\partial x \partial y} \right), \tag{16}$$

$$\frac{\partial^2 v^*}{\partial t^2} = \bar{v}^* + \frac{1}{\rho^*} f_y^* \qquad \text{with} \qquad \bar{v}^* = \frac{\mu^*}{\rho^*} \nabla^2 v^* + \frac{(\mu^* + \lambda^*)}{\rho^*} \left(\frac{\partial^2 v^*}{\partial y^2} + \frac{\partial^2 u^*}{\partial x \partial y} \right), \tag{17}$$

$$\frac{\partial^2 u^{**}}{\partial t^2} = \bar{u}^{**} + \frac{1}{\rho^{**}} f_x^{**} \qquad \text{with} \qquad \bar{u}^{**} = \frac{\mu^{**}}{\rho^{**}} \nabla^2 u^{**} + \frac{(\mu^{**} + \lambda^{**})}{\rho^{**}} \left(\frac{\partial^2 u^{**}}{\partial x^2} + \frac{\partial^2 v^{**}}{\partial x \partial y} \right), \tag{18}$$

$$\frac{\partial^2 v^{**}}{\partial t^2} = \bar{v}^{**} + \frac{1}{\rho^{**}} f_y^{**} \qquad \text{with} \qquad \bar{v}^{**} = \frac{\mu^{**}}{\rho^{**}} \nabla^2 v^{**} + \frac{(\mu^{**} + \lambda^{**})}{\rho^{**}} \left(\frac{\partial^2 v^{**}}{\partial y^2} + \frac{\partial^2 u^{**}}{\partial x \partial y} \right), \tag{19}$$

Inserting Eqs. (16)-(19) into Eq. (14) we will get:

$$e_{j} = h^{2} \left\{ \sum_{p=1}^{9} m_{j,p} \left[a_{p} \bar{u}_{p}^{*} + (1 - a_{p}) \bar{u}_{p}^{**} \right] + \sum_{p=1}^{9} \bar{m}_{j,p} \left[a_{p} \bar{v}_{p}^{*} + (1 - a_{p}) \bar{v}_{p}^{**} \right] \right\}$$

$$+ \sum_{p=1}^{9} k_{j,p} \left[a_{p} u_{p}^{*} + (1 - a_{p}) u_{p}^{**} \right] + \sum_{p=1}^{9} \bar{k}_{j,p} \left[a_{p} v_{p}^{*} + (1 - a_{p}) v_{p}^{**} \right]$$

$$+ \left[\sum_{m=1}^{N_{G}} q_{1,m} (u_{G,m}^{*} - u_{G,m}^{**}) + \sum_{m=1}^{N_{G}} q_{2,m} (v_{G,m}^{*} - v_{G,m}^{**}) + \sum_{m=1}^{N_{G}} hq_{3,m} (t_{x(G,m)}^{*} - t_{x(G,m)}^{**}) + \sum_{m=1}^{N_{G}} hq_{4,m} (t_{y(G,m)}^{*} - t_{y(G,m)}^{**}) \right]$$

$$+ e_{j}^{f}, \qquad j = 1, 2,$$

$$(20)$$

where in Eq. (20) we moved all terms with the body forces to the term e_i^f as follows:

$$e_{j}^{f} = -\bar{f}_{j,5} + h^{2} \left\{ \sum_{p=1}^{9} m_{j,p} \left[a_{p} \frac{f_{p,x}^{*}}{\rho^{*}} + (1 - a_{p}) \frac{f_{p,x}^{**}}{\rho^{**}} \right] + \sum_{p=1}^{9} \bar{m}_{j,p} \left[a_{p} \frac{f_{p,y}^{*}}{\rho^{*}} + (1 - a_{p}) \frac{f_{p,y}^{**}}{\rho^{**}} \right] \right\}, \qquad j = 1, 2.$$
 (21)

Here, $f_{p,x}^{*(**)} = f_x^{*(**)}(x_p, y_p, t)$ and $f_{p,y}^{*(**)} = f_y^{*(**)}(x_p, y_p, t)$ with x_p and y_p given by Eq. (9). Equating to zero $e_j^f = 0$, we can define the load term $\bar{f}_{j,5}$ due to the body forces in the stencil equations:

$$\bar{f}_{j,5} = h^2 \left\{ \sum_{p=1}^9 m_{j,p} \left[a_p \frac{f_{p,x}^*}{\rho^*} + (1 - a_p) \frac{f_{p,x}^{**}}{\rho^{**}} \right] + \sum_{p=1}^9 \bar{m}_{j,p} \left[a_p \frac{f_{p,y}^*}{\rho^*} + (1 - a_p) \frac{f_{p,y}^{**}}{\rho^{**}} \right] \right\}, \qquad j = 1, 2,$$
 (22)

as well as we will get that the local truncation errors e_j is independent of the body forces. As can be seen from Eq. (22), the load term $\bar{f}_{j,5}$ depends on the stencil coefficients $m_{j,p}$, $\bar{m}_{j,p}$ (p=1,2,...,9) that should be first calculated as described in the next Section 2.3. Then, the load term $\bar{f}_{j,5}$ is calculated according to Eq. (22).

Remark 6. It is interesting to mention that in our previous papers on OLTEM for the time-dependent PDEs (e.g., see [44, 46, 48, 51]), the load term $\bar{f}_{j,5}$ in the stencil equations is calculated in terms of a Taylor series expansion of the loading (source) term of the corresponding PDEs. This leads to a long expression for $\bar{f}_{j,5}$ with the high-order spatial derivatives. Here, we have found that for time-dependent PDEs we can use another procedure for OLTEM without the use of a Taylor series expansion. We can obtain a much simpler expression for the load term (see Eq. 22) that also requires smaller computation time.

2.3. The calculation of the stencil coefficients

The calculation of the stencil coefficients is based on the minimization of the order and the leading terms in a Taylor series expansion of the local truncation error of the stencil equations. In order to represent the local truncation error e_j as a Taylor series, let us expand the exact solution at the grid points and the selected N_G interface points in Eq. (20) into a Taylor series at small $h \ll 1$ in the vicinity of the central grid point with the coordinates x_5 and y_5 (see Figure 1) as follows:

$$w = w_5 + \frac{\partial w_5}{\partial x} \left[c_{x,j} h \right] + \frac{\partial w_5}{\partial y} \left[c_{y,j} b_y h \right] + \frac{\partial^2 w_5}{\partial x^2} \frac{\left[c_{x,j} h \right]^2}{2!} + \frac{\partial^2 w_5}{\partial y^2} \frac{\left[c_{y,j} b_y h \right]^2}{2!} + 2 \frac{\partial^2 w_5}{\partial x \partial y} \frac{\left[c_{x,j} h \right] \left[c_{y,j} b_y h \right]}{2!} + \dots$$

$$(23)$$

In Eq. (23) the function w is u_j^* , u_j^{**} , v_j^* , v_j^{**} with $c_{x,j} = r_{x,j}$, $c_{y,j} = r_{y,j}$ (j = 1, 2, ..., 9) as well as the function w is $u_{G,j}^*$, $u_{G,j}^*$, $u_{G,j}^{**}$, $u_{G,j}$

$$\begin{split} e_{j} &= b_{j,1} u_{5}^{*} + b_{j,2} u_{5}^{**} + b_{j,3} v_{5}^{*} + b_{j,4} v_{5}^{**} + h \left(b_{j,5} \frac{\partial u_{5}^{*}}{\partial x} + b_{j,6} \frac{\partial u_{5}^{*}}{\partial x} + b_{j,7} \frac{\partial v_{5}^{*}}{\partial x} + b_{j,9} \frac{\partial v_{5}^{*}}{\partial x} + b_{j,9} \frac{\partial u_{5}^{*}}{\partial y} + b_{10} \frac{\partial u_{5}^{**}}{\partial y} + b_{j,11} \frac{\partial v_{5}^{*}}{\partial y} + b_{j,12} \frac{\partial v_{5}^{**}}{\partial y} \right) \\ &+ h^{2} \left(b_{j,13} \frac{\partial^{2} u_{5}^{*}}{\partial x^{2}} + b_{j,14} \frac{\partial^{2} u_{5}^{**}}{\partial x^{2}} + b_{j,15} \frac{\partial^{2} v_{5}^{*}}{\partial x^{2}} + b_{j,16} \frac{\partial^{2} v_{5}^{**}}{\partial x^{2}} + b_{j,17} \frac{\partial^{2} u_{5}^{*}}{\partial x^{2}} + b_{j,18} \frac{\partial^{2} u_{5}^{**}}{\partial x^{2}} \right) \\ &+ b_{j,19} \frac{\partial^{2} v_{5}^{*}}{\partial x \partial y} + b_{j,20} \frac{\partial^{2} v_{5}^{*}}{\partial x \partial y} + b_{j,21} \frac{\partial^{2} u_{5}^{*}}{\partial y^{2}} + b_{j,22} \frac{\partial^{2} u_{5}^{*}}{\partial y^{2}} + b_{j,22} \frac{\partial^{2} v_{5}^{*}}{\partial y^{2}} + b_{j,23} \frac{\partial^{2} v_{5}^{*}}{\partial y^{2}} \right) \\ &+ h^{3} \left(b_{j,25} \frac{\partial^{3} u_{5}^{*}}{\partial x^{3}} + b_{j,20} \frac{\partial^{3} u_{5}^{*}}{\partial x^{3}} + b_{j,22} \frac{\partial^{3} v_{5}^{*}}{\partial x^{3}} + b_{j,29} \frac{\partial^{3} u_{5}^{*}}{\partial x^{2} \partial y} + b_{j,30} \frac{\partial^{3} u_{5}^{*}}{\partial x^{2} \partial y} + b_{j,31} \frac{\partial^{3} v_{5}^{*}}{\partial x^{2} \partial y} + b_{j,32} \frac{\partial^{3} v_{5}^{**}}{\partial x^{2} \partial y} \right) \\ &+ b_{j,33} \frac{\partial^{3} u_{5}^{*}}{\partial x \partial y^{2}} + b_{j,35} \frac{\partial^{3} u_{5}^{*}}{\partial x \partial y^{2}} + b_{j,36} \frac{\partial^{3} v_{5}^{*}}{\partial x \partial y^{2}} + b_{j,37} \frac{\partial^{3} u_{5}^{*}}{\partial y^{3}} + b_{j,38} \frac{\partial^{3} u_{5}^{*}}{\partial y^{3}} + b_{j,40} \frac{\partial^{3} v_{5}^{*}}{\partial y^{3}} \right) \\ &+ h^{4} \left(b_{j,41} \frac{\partial^{4} u_{5}^{*}}{\partial x^{4}} + \dots + b_{j,60} \frac{\partial^{4} v_{5}^{*}}{\partial y^{4}} \right) + h^{5} \left(b_{j,61} \frac{\partial^{5} u_{5}^{*}}{\partial x^{5}} + \dots + b_{j,84} \frac{\partial^{5} v_{5}^{*}}{\partial y^{5}} \right) + h^{6} \left(b_{j,85} \frac{\partial^{6} u_{5}^{*}}{\partial x^{6}} + \dots + b_{j,112} \frac{\partial^{6} u_{5}^{*}}{\partial y^{6}} \right) + O(h^{7}), \quad j = 1,2 \end{split}$$

where the coefficients $b_{j,p}$ (j=1, 2, p=1,2,...,112) are expressed in terms of the coefficients $m_{j,i}$, $\bar{m}_{j,i}$, $k_{j,i}$, $\bar{k}_{j,i}$ (i=1,2,...,9) and $q_{1,m}$, $q_{2,m}$, $q_{3,m}$, $q_{4,m}$ (m=1,2,...,5); see Appendix A and B.

Below we first show the derivation of the stencil coefficients for the heterogeneous stencil that is divided by the interface and includes the grid points belonging to different materials. Then, we show the simplification of the general approach to the case of the homogeneous stencil with the grid points belonging to the same material and no interfaces.

2.3.1. 9-Point stencils for heterogeneous materials with an irregular interface

The formulas presented below can be used for the first j = 1 and second j = 2 stencils (they should be separately considered for j = 1 and j = 2). In order to minimize the order of the local truncation error e_j in Eq. (24), we will zero the first 24 coefficients $b_{j,p}$ in Eq. (24) up to the second order with respect to h; i.e.,

$$b_{j,p} = 0, p = 1, 2, ..., 24.$$
 (25)

Then, in order to have a sufficient number of equations for the calculation of the 56 stencil coefficients of each stencil including $m_{j,i}$, $\bar{m}_{j,i}$, $k_{j,i}$, $\bar{k}_{j,i}$ (i=1,2,...,9) and $q_{1,m}$, $q_{2,m}$, $q_{3,m}$, $q_{4,m}$ (m=1,2,...,5), we use the least square method for the minimization of coefficients $b_{j,p}$ related to the third, fourth, fifth and sixth orders of the local truncation error with the following residual R_i :

$$R_{j} = \sum_{p=25}^{40} b_{j,p}^{2} + h_{1} \sum_{p=41}^{60} b_{j,p}^{2} + h_{2} \sum_{p=61}^{84} b_{j,p}^{2} + h_{3} \sum_{p=85}^{112} b_{j,p}^{2},$$
 (26)

where h_1 , h_2 and h_3 are the weighting factors to be selected (e.g., the numerical experiments show that $h_1 = h_2 = h_3 = 0.1$ yield accurate results). In order to minimize the residual R_j with the constraints given by Eq. (25), we can form a new residual \bar{R}_j with the Lagrange multipliers λ_l :

$$\bar{R}_{j} = \sum_{l=1}^{24} \lambda_{l} b_{j,l} + \sum_{p=25}^{40} b_{j,p}^{2} + h_{1} \sum_{p=41}^{60} b_{j,p}^{2} + h_{2} \sum_{p=61}^{84} b_{j,p}^{2} + h_{3} \sum_{p=85}^{112} b_{j,p}^{2}.$$

$$(27)$$

The residual \bar{R}_j is a quadratic function of the stencil coefficients $m_{j,i}$, $\bar{m}_{j,i}$, $k_{j,i}$, $\bar{k}_{j,i}$ (i=1,2,...,9) and $q_{1,m}$, $q_{2,m}$, $q_{3,m}$, $q_{4,m}$ (m=1,2,...,5), and a linear function of the Lagrange multipliers λ_l ; i.e., $\bar{R}_j = \bar{R}_j(m_{j,i},\bar{m}_{j,i},k_{j,i},\bar{k}_{j,i},q_{p,m},\lambda_l)$ (p=1,2,...,4). In order to minimize the residual $\bar{R}_j = \bar{R}_j(m_{j,i},\bar{m}_{j,i},k_{j,i},\bar{k}_{j,i},q_{p,m},\lambda_l)$, the following equations based on the least square method for the residual \bar{R}_j can be written down:

$$\frac{\partial \bar{R}_{j}}{\partial m_{j,i}} = 0, \qquad \frac{\partial \bar{R}_{j}}{\partial \bar{m}_{j,i}} = 0, \qquad \frac{\partial \bar{R}_{j}}{\partial k_{j,i}} = 0, \qquad \frac{\partial \bar{R}_{j}}{\partial \bar{k}_{j,i}} = 0,
\frac{\partial \bar{R}_{j}}{\partial q_{1,m}} = 0, \qquad \frac{\partial \bar{R}_{j}}{\partial q_{2,m}} = 0, \qquad \frac{\partial \bar{R}_{j}}{\partial q_{3,m}} = 0, \qquad \frac{\partial \bar{R}_{j}}{\partial q_{4,m}} = 0, \qquad \frac{\partial \bar{R}_{j}}{\partial \lambda_{l}} = 0,
i = 1, 2, ..., 9, \qquad m = 1, 2, ..., 5, \qquad l = 1, 2, ..., 24,$$
(28)

where equations $\frac{\partial \bar{R}_1}{\partial k_{1,5}} = \frac{\partial \bar{R}_1}{\partial k_{1,5}} = 0$ should be replaced by $k_{1,5} = 1$ and $\bar{k}_{1,5} = 0$ for the first stencil with j = 1 as well as $\frac{\partial \bar{R}_2}{\partial k_{2,5}} = 0$ should be replaced by $k_{2,5} = 0$ and $\bar{k}_{2,5} = 1$ for the second stencil with j = 2; see Remark 3. Eq. (28) forms a system of 80 linear algebraic equations with respect to 56 unknown coefficients $m_{j,i}$, $\bar{m}_{j,i}$, $k_{j,i}$, $\bar{k}_{j,i}$ (i = 1, 2, ..., 9) and $q_{1,m}$, $q_{2,m}$, $q_{3,m}$, $q_{4,m}$ (m = 1, 2, ..., 5) as well as 24 Lagrange multipliers λ_l (l = 1, 2, ..., 24). Solving these linear algebraic

equations numerically, we can find the coefficients $m_{i,i}, \bar{m}_{i,i}, k_{i,i}, k_{j,i}$ (i = 1, 2, ..., 9) for the 9-point uniform stencils as well as $q_{1,m}$, $q_{2,m}$, $q_{3,m}$, $q_{4,m}$ (m = 1, 2, ..., 5). As can be seen from Eq. (28), the interface conditions that introduce the additional terms in the expressions for the coefficients $b_{j,p}$ (see the terms with the $q_{1,m}$, $q_{2,m}$, $q_{3,m}$, $q_{4,m}$ coefficients in Appendix A) affect the calculation of the stencil coefficients $m_{j,i}$, $\bar{m}_{j,i}$, $k_{j,i}$, $k_{j,i}$ (i = 1, 2, ..., 9) through the coefficients $b_{j,p}$. We should also note that similar to the imposition of the constraint $k_{1,5} = 1$, we can impose the constraint for any stencils coefficients (e.g., for the diagonal coefficient $m_{1,5}$ if it is very small).

Remark 7. To estimate the computational costs for the solution of 80 linear algebraic equations formed by Eq. (28) for the 9-point stencils, we solved 10³ such systems with the general MATLAB solver on a desktop computer (Processor: Intel (R) Core(TN) i9-9900 CPU @3.10Hz 3.10 HZ). The computation "wall" time was T = 2.232s for 10^3 systems or the average time for one system was 0.002232s for the 9-point stencils. Because the coefficients $m_{j,i}$, $\bar{m}_{j,i}$, $k_{j,i}$, $\bar{k}_{j,i}$ (i = 1, 2, ..., 9) are independently calculated for different grid points, the computation time of their calculation for different grid points can be significantly reduced on modern parallel computers. This means that for large global systems of semi-discrete equations, the computation time for the calculation of the coefficients $m_{i,i}, \bar{m}_{i,i}, k_{i,i}, k_{i,i}$ (i = 1, 2, ..., 9) is very small compared to that for the solution of the global system of semi-discrete equations. We should mention that the coefficients $q_{1,m}, q_{2,m}, q_{3,m}, q_{4,m}$ as well as the Lagrange multipliers λ_l in the local system of equations, Eq. (28), are not used in the global system of semi-discrete equations at all.

Remark 8. It is interesting to mention that the stencil coefficients can be also derived using a Taylor series expansion in the vicinity of the interface point with the coordinates x_G and y_G in Eqs. (23) and (24) instead of the central grid point with the coordinates x_5 and y_5 .

2.3.2. Homogeneous materials (no interface)

For homogeneous materials all a_i (i = 1, 2, ..., 9) coefficients are $a_i = 1$ (see Eq. 12 if we consider material *) as well as all $q_{1,j} = q_{2,j} = q_{3,j} = q_{4,j} = 0$ (j = 1, 2, ..., 5) coefficients are zero. The case of material ** can be similarly treated. For material * the local truncation error, Eq. (24), does not include the terms with symbol **; i.e., the corresponding terms $b_{2i} = 0$ (i = 1, 2, ..., 56) in Eq. (24). Then, the local system of equations, Eq. (28), reduces to the following 48 algebraic equations for the 36 stencil coefficients $m_{i,i}$, $\bar{m}_{i,i}$, $k_{i,i}$, $k_{i,i}$ (i = 1, 2, ..., 9) and 12 Lagrange multipliers λ_{2l-1} (l = 1, 2, ..., 12):

$$\begin{split} \frac{\partial \bar{R}_{j}}{\partial m_{j,i}} &= 0, \qquad \frac{\partial \bar{R}_{j}}{\partial \bar{m}_{j,i}} = 0, \qquad \frac{\partial \bar{R}_{j}}{\partial k_{j,i}} = 0, \qquad \frac{\partial \bar{R}_{j}}{\partial \bar{k}_{j,i}} = 0, \\ \frac{\partial \bar{R}_{j}}{\partial \lambda_{2l-1}} &= 0, \quad i = 1, 2, ..., 9, \qquad l = 1, 2, ..., 12, \end{split}$$

(29)

where similar to Section 2.3.1, equations $\frac{\partial \bar{R}_1}{\partial k_{1.5}} = \frac{\partial \bar{R}_1}{\partial \bar{k}_{1.5}} = 0$ should be replaced by $k_{1,5}=1$ and $\bar{k}_{1,5}=0$ for the first stencil with j=1 as well as $\frac{\partial \bar{R}_2}{\partial k_{2,5}}=\frac{\partial \bar{R}_2}{\partial k_{2,5}}=0$ should be replaced by $k_{2,5} = 0$ and $\bar{k}_{2,5} = 1$ for the second stencil with i=2; see Remark 3. We should mention that the explicit values of the stencil coefficients for homogeneous materials with Poisson ratio $\nu = 0.3$ are given in our paper [46]. The stencil coefficients of OLTEM for homogeneous materials provide the fourth order of the local truncation error, Eq. (24); i.e., the order of the local truncation error cannot exceed four for any 9-point uniform stencils independent of the method used for their derivation (the finite element method, the finite volume method, the finite difference method, or any other method). The fourth order of the local truncation error corresponds to the second order of accuracy for the global numerical solution (e.g., see our paper [46]) and is the same as that for linear finite elements. These results are different from the application of OLTEM to the scalar wave equation for which at the same 9-point stencils the accuracy was improved by two orders compared to linear finite elements; see [42].

As can be seen, the presented procedure provides the third order of the local truncation error for the 9-point uniform stencils with the general geometry of the interface. The 9-point uniform stencils of OLTEM for homogeneous materials (without interface) provide the fourth order of the local truncation error. This leads to the second order of accuracy of global solutions; see the numerical examples below. Moreover, due to the minimization of the leading highorder terms $b_{i,p}$ of the local truncation error with Eqs. (28) and (29), at the same numbers of degrees of freedom and at the engineering accuracy, OLTEM with irregular interfaces yields more accurate results than those obtained by highorder finite elements (up to the third order) with much wider stencils; see the numerical examples below.

The global system of semi-discrete equations includes the 9-point stencils for homogeneous materials without interfaces and the 9-point stencils for heterogeneous materials with interfaces between different materials (see Figure 1) for all internal grid points located inside the domain. OLTEM does not use the unknowns at the interfaces and the global system of semi-discrete equations has the same structures of the global matrices for homogeneous and heterogeneous materials (see Eq. 12), the difference is only in the values of the stencil coefficients $m_{i,i}$, $\bar{m}_{i,i}$, $k_{i,i}$, $\bar{k}_{i,i}$ of the global matrices).

2.4. The simplification of OLTEM for the diagonal global mass matrix

OLTEM derived in Sections 2.1 - 2.3 leads to the non-diagonal global mass matrix because the stencil coefficients $m_{j,i}$, $\bar{m}_{j,i}$ (i = 1, 2, ..., 9) are generally non-zero. However, OLTEM can be easily derived for the diagonal global mass matrix. In this case in Eqs. (12)–(14), (20)–(22) of the previous Sections we should zero all stencil coefficients $m_{j,i}$ $\bar{m}_{i,i} = 0$ (i = 1, 2, ..., 9) except $m_{1,5} \neq 0$ for the first stencil

with j=1 and $\bar{m}_{2,5}\neq 0$ for the second stencil with j=2 as well as the first two formulas in Eqs. (28) and (29) should be replaced by $\frac{\partial \bar{R}_1}{\partial m_{1.5}} = 0$ and $\frac{\partial \bar{R}_2}{\partial \bar{m}_{2.5}} = 0$.

3. OLTEM for post-processing of numerical results: calculations of spatial derivatives

For elastodynamics problems the accurate calculations of stresses is a very important part of a numerical technique because stresses define many mechanical phenomenon; e.g., crack propagation in fracture mechanics. Therefore, after the displacement calculation, many computer codes include special post-processing procedures for the stress calculation. The stresses are defined by Hooke's law in terms of the spatial derivatives of the displacements. Here we show the application of OLTEM with the compact 9-point stencils (the same as we used in the previous sections; see also Figure 1) for the calculation of the spatial derivatives of the displacements $\frac{\partial u^{num}}{\partial x}$, $\frac{\partial u^{num}}{\partial y}$, $\frac{\partial v^{num}}{\partial x}$, $\frac{\partial v^{num}}{\partial y}$. Using these derivatives, the normal s_x , s_y and shear s_{xy} stresses are easily calculated according to Hooke's law:

$$s_x = (2\mu + \lambda)\frac{\partial u}{\partial x} + \mu \frac{\partial v}{\partial y}, \qquad s_y = (2\mu + \lambda)\frac{\partial v}{\partial y} + \mu \frac{\partial u}{\partial x}, \qquad s_{xy} = \mu \left(\frac{\partial u}{\partial y} + \frac{\partial v}{\partial x}\right).$$
 (30)

Because the calculations of the four spatial derivatives of the displacements are similar then the procedure for $\frac{\partial u^{num}}{\partial x}$ is shown in detail only.

The compact 9-point stencils for the calculation of $\frac{\partial u^{num}}{\partial x}$ at the central stencil grid point with the coordinates x_5 and y_5 (see Figure 1) can be selected similar to Eq. (12) as follows:

$$-\left[a_{5}\frac{\partial u_{5}^{*,num}}{\partial x}+(1-a_{5})\frac{\partial u_{5}^{**,num}}{\partial x}\right]h$$

$$+h^{2}\left\{\sum_{p=1}^{9}m_{p}\left[a_{p}\frac{d^{2}u_{p}^{*,num}}{dt^{2}}+(1-a_{p})\frac{d^{2}u_{p}^{**,num}}{dt^{2}}\right]+\sum_{p=1}^{9}\bar{m}_{p}\left[a_{p}\frac{d^{2}v_{p}^{*,num}}{dt^{2}}+(1-a_{p})\frac{d^{2}v_{p}^{**,num}}{dt^{2}}\right]\right\}$$

$$+\sum_{p=1}^{9}k_{p}\left[a_{p}u_{p}^{*,num}+(1-a_{p})u_{p}^{**,num}\right]+\sum_{p=1}^{9}\bar{k}_{p}\left[a_{p}v_{p}^{*,num}+(1-a_{p})v_{p}^{**,num}\right]=\bar{f}_{5},$$
(31)

where $a_5 = 1$ if the central stencil point belongs to material * and $a_5 = 0$ if the central stencil point belongs to material **. We should mention that in contrast to known post-processing procedures (e.g., used with finite elements), in the proposed approach the calculation of the spatial derivative $\frac{\partial u}{\partial x}$ depends not only on the displacement u but also on the displacement v as well as their second order time derivatives $\frac{\partial^2 u}{\partial t^2}$ and $\frac{\partial^2 v}{\partial t^2}$. The local truncation error e for Eq. (31) can be obtained by the replacement of the numerical solution $u_p^{*,num}$, $u_p^{**,num}$, $v_p^{*,num}$ and $v_p^{**,num}$ in Eq. (31) by the exact solutions u_p^* , u_p^{**} , v_p^* and ν_p^{**} :

$$e = -\left[a_{5}\frac{\partial u_{5}^{*}}{\partial x} + (1 - a_{5})\frac{\partial u_{5}^{**}}{\partial x}\right]h + h^{2}\left\{\sum_{p=1}^{9}m_{p}\left[a_{p}\frac{d^{2}u_{p}^{*}}{dt^{2}} + (1 - a_{p})\frac{d^{2}u_{p}^{**}}{dt^{2}}\right] + \sum_{p=1}^{9}\bar{m}_{p}\left[a_{p}\frac{d^{2}v_{p}^{*}}{dt^{2}} + (1 - a_{p})\frac{d^{2}v_{p}^{**}}{dt^{2}}\right]\right\} + \sum_{p=1}^{9}k_{p}\left[a_{p}u_{p}^{*} + (1 - a_{p})u_{p}^{**}\right] + \sum_{p=1}^{9}\bar{k}_{p}\left[a_{p}v_{p}^{*} + (1 - a_{p})v_{p}^{**}\right] - \bar{f}_{5}.$$

$$(32)$$

We should note that in Eq. (32) we do not use index "j" for the local truncation error e and for the stencil coefficients m_i , \bar{m}_i , k_i , \bar{k}_i (i=1,2,...,9) because for the calculation of $\frac{\partial u^{num}}{\partial x}$ we consider just one stencil equation. Similar to Eq. (14) in Section 2, we will include the interface conditions for the exact solution at the same small number N_G of the interface points into the expression for the local truncation error in Eq. (32) as follows:

$$e = -\left[a_{5}\frac{\partial u_{5}^{*}}{\partial x} + (1 - a_{5})\frac{\partial u_{5}^{**}}{\partial x}\right]h + h^{2}\left\{\sum_{p=1}^{9}m_{p}\left[a_{p}\frac{d^{2}u_{p}^{*}}{dt^{2}} + (1 - a_{p})\frac{d^{2}u_{p}^{**}}{dt^{2}}\right] + \sum_{p=1}^{9}\bar{m}_{p}\left[a_{p}\frac{d^{2}v_{p}^{*}}{dt^{2}} + (1 - a_{p})\frac{d^{2}v_{p}^{**}}{dt^{2}}\right]\right\}$$

$$+ \sum_{p=1}^{9}k_{p}\left[a_{p}u_{p}^{*} + (1 - a_{p})u_{p}^{**}\right] + \sum_{p=1}^{9}\bar{k}_{p}\left[a_{p}v_{p}^{*} + (1 - a_{p})v_{p}^{**}\right]$$

$$+ \left[\sum_{m=1}^{N_{G}}q_{1,m}(u_{G,m}^{*} - u_{G,m}^{**}) + \sum_{m=1}^{N_{G}}q_{2,m}(v_{G,m}^{*} - v_{G,m}^{**}) + \sum_{m=1}^{N_{G}}hq_{3,m}(t_{x(G,m)}^{*} - t_{x(G,m)}^{**}) + \sum_{m=1}^{N_{G}}hq_{4,m}(t_{y(G,m)}^{*} - t_{y(G,m)}^{**})\right] - \bar{f}_{5},$$

$$(33)$$

see the corresponding explanations in Section 2.1. For the accurate calculation of the derivative $\frac{\partial u^{num}}{\partial x}$, we should minimize the local truncation error e in Eq. (33). Repeating the procedure described in Section 2 we can derive the load term \bar{f}_5 that



is also calculated according to Eq. (22). Then, the local truncation error in space e in Eq. (24) is modified in this case as follows:

Calculate the derivative $\frac{\partial u^{num}}{\partial x}$ from Eq. (31) for each internal grid point as follows:

$$e = b_{1}u_{5}^{*} + b_{2}u_{5}^{**} + b_{3}v_{5}^{*} + b_{4}v_{5}^{**} + h\left((b_{5} - a_{5})\frac{\partial u_{5}^{*}}{\partial x} + (b_{6} - (1 - a_{5}))\frac{\partial u_{5}^{**}}{\partial x} + b_{7}\frac{\partial v_{5}^{*}}{\partial x} + b_{8}\frac{\partial v_{5}^{**}}{\partial x} + b_{9}\frac{\partial u_{5}^{*}}{\partial y} + b_{10}\frac{\partial u_{5}^{**}}{\partial y}\right) + h_{11}\frac{\partial v_{5}^{*}}{\partial y} + b_{12}\frac{\partial^{2}u_{5}^{**}}{\partial y} + b_{15}\frac{\partial^{2}v_{5}^{*}}{\partial x^{2}} + b_{16}\frac{\partial^{2}v_{5}^{**}}{\partial x^{2}} + b_{17}\frac{\partial^{2}u_{5}^{*}}{\partial x\partial y} + b_{18}\frac{\partial^{2}u_{5}^{**}}{\partial x\partial y} + b_{18}\frac{\partial^{2}u_{5}^{**}}{\partial x\partial y} + b_{19}\frac{\partial^{2}v_{5}^{*}}{\partial x\partial y} + b_{20}\frac{\partial^{2}v_{5}^{**}}{\partial x\partial y} + b_{21}\frac{\partial^{2}u_{5}^{*}}{\partial y^{2}} + b_{22}\frac{\partial^{2}u_{5}^{**}}{\partial y^{2}} + b_{23}\frac{\partial^{2}v_{5}^{*}}{\partial y^{2}} + b_{24}\frac{\partial^{2}v_{5}^{**}}{\partial y^{2}} + \dots$$

$$(34)$$

where the coefficients b_p (p = 1, 2, ...) are expressed in terms of the coefficients m_i , \bar{m}_i , k_i , \bar{k}_i (i = 1, 2, ..., 9) $q_{1,j}, q_{2,j}, q_{3,j}, q_{4,j}$ (j = 1, 2, ..., 5). The coefficients b_n (p = 1, 2, ...) are exactly the same as those in Eq. (24) and are given in Appendix A. The difference between Eqs. (24) and (34) is just in two coefficients before the derivatives $\frac{\partial u_5^*}{\partial x}$ and $\frac{\partial u_5^{**}}{\partial x}$:

$$\bar{b}_5 = b_5 - a_5, \qquad \bar{b}_6 = b_6 - (1 - a_5), \tag{35}$$

where \bar{b}_5 and \bar{b}_6 are the coefficients in Eq. (34). For homogeneous materials (without interface), the coefficients $q_{1,j}$ = $q_{2,j} = q_{3,j} = q_{4,j} = 0$ (j = 1, 2, ..., 5) are zero and the stencils coefficients m_i , \bar{m}_i , k_i , \bar{k}_i (i = 1, 2, ..., 9) can be found similar to those in Section 2.3.2 using Eq. (29). The stencil coefficients of OLTEM for homogeneous materials provide the fourth order of the local truncation error e. For heterogeneous materials with interfaces, the stencil coefficients m_i \bar{m}_i , k_i , k_i (i = 1, 2, ..., 9) and $q_{1,j}$, $q_{2,j}$, $q_{3,j}$, $q_{4,j}$ (j = 1, 2, ..., 5)are calculated similar to those in Section 2.3.1 from 80 linear algebraic equations formed by Eq. (28). In contrast to Sections 2.3.1-2.3.2, in Eqs. (28) and (29) we do not use the condition that $k_{1,5} = 1$ and $k_{1,5} = 0$ for the first stencil with j=1 and $k_{2,5}=0$ and $k_{2,5}=1$ for the second stencil with j=2; i.e., we do not modify Eqs. (28) and (29). We also use Eq. (35) instead of b_5 and b_6 . Due to Eq. (25), the stencil coefficients for heterogeneous materials provide the 3-rd order of accuracy for the local truncation error *e*.

To summarize, for the calculation of the derivative $\frac{\partial u^{num}}{\partial x}$ using OLTEM with the 9-point stencils, we should follow the following procedure:

- Calculate the stencil coefficients m_i , \bar{m}_i , k_i , \bar{k}_i (i = 1, 2, ..., 9) and $q_{1,j}, q_{2,j}, q_{3,j}, q_{4,j}$ (j = 1, 2, ..., 5)for each internal grid point as described above in Section for homogeneous (without interfaces and $q_{1,j} = q_{2,j} = q_{3,j} = q_{4,j} = 0$) and heterogeneous (with interfaces) materials.
- Using these stencil coefficients, calculate the right-hand side \bar{f}_5 in Eq. (31) for each internal grid point using Eq. (22).

$$\frac{\partial u_{5}^{*,num}}{\partial x} = h \left\{ \sum_{p=1}^{9} m_{p} \left[a_{p} \frac{d^{2} u_{p}^{*,num}}{dt^{2}} + (1 - a_{p}) \frac{d^{2} u_{p}^{**,num}}{dt^{2}} \right] + \sum_{p=1}^{9} \bar{m}_{p} \left[a_{p} \frac{d^{2} v_{p}^{*,num}}{dt^{2}} + (1 - a_{p}) \frac{d^{2} v_{p}^{**,num}}{dt^{2}} \right] \right\} + \frac{1}{h} \left\{ \sum_{p=1}^{9} k_{p} \left[a_{p} u_{p}^{*,num} + (1 - a_{p}) u_{p}^{**,num} \right] + \sum_{p=1}^{9} \bar{k}_{p} \left[a_{p} v_{p}^{*,num} + (1 - a_{p}) v_{p}^{**,num} \right] - \bar{f}_{5} \right\}, \tag{36}$$

if the central stencil point belongs to material $*(a_5 = 1)$

$$\begin{split} \frac{\partial u_{5}^{**,num}}{\partial x} &= h \bigg\{ \sum_{p=1}^{9} m_{p} \bigg[a_{p} \frac{d^{2} u_{p}^{*,num}}{dt^{2}} + (1 - a_{p}) \frac{d^{2} u_{p}^{**,num}}{dt^{2}} \bigg] \\ &+ \sum_{p=1}^{9} \bar{m}_{p} \bigg[a_{p} \frac{d^{2} v_{p}^{*,num}}{dt^{2}} + (1 - a_{p}) \frac{d^{2} v_{p}^{**,num}}{dt^{2}} \bigg] \bigg\} \\ &+ \frac{1}{h} \bigg\{ \sum_{p=1}^{9} k_{p} \bigg[a_{p} u_{p}^{*,num} + (1 - a_{p}) u_{p}^{**,num} \bigg] \\ &+ \sum_{p=1}^{9} \bar{k}_{p} \bigg[a_{p} v_{p}^{*,num} + (1 - a_{p}) v_{p}^{**,num} \bigg] - \bar{f}_{5} \bigg\}, \end{split}$$

if the central stencil point belongs to material ** $(a_5 = 0)$.

The calculation of the derivatives $\frac{\partial u^{num}}{\partial v}$, $\frac{\partial v^{num}}{\partial x}$ and $\frac{\partial v^{num}}{\partial v}$ can be done similar to the calculation of the derivative $\frac{\partial u^{num}}{\partial x}$ as described above.

Remark 9. If any of the grid points included into the stencil is located on the boundary with the Dirichlet boundary conditions then for this point p in Eqs. (36) and (37) the exact values of u_p^* or u_p^{**} , v_p^* or v_p^{**} defined by the boundary conditions are used. In the case of the Neumann boundary conditions, the procedure can be modified similar to that in our paper [55] for OLTEM with irregular boundaries and the Neumann boundary conditions.

Remark 10. The described post-processing procedure can be equally applied to OLTEM with the diagonal mass matrix.

It is interesting to note that for homogeneous materials the post-processing procedure described above can be also used for the calculation of the spatial derivatives without the application of the partial differential equation as in other post-processing techniques (e.g., see [52–54] for finite and isogeometric elements). Let us assume that we can calculate the derivative $\frac{\partial u^{num}}{\partial x}$ at the internal grid point in terms of the values of the displacement u^{num} at the neighboring grid points. For simplicity, we will use a uniform Cartesian mesh and 9 grid points for the calculation of the derivative $\frac{\partial u^{num}}{\partial x}$ at the central grid point (see Figure 1a) as follows:

$$-h\frac{\partial u_5^{num}}{\partial x} + \sum_{p=1}^9 k_p u_p^{num} = 0$$
 (38)

with the following local truncation error:

$$e = -h\frac{\partial u_5}{\partial x} + \sum_{p=1}^{9} k_p u_p. \tag{39}$$

Using the procedure described in Section 2.3 without the use of the elastodynamics equations, Eqs. (16)–(19), and zeroing the corresponding coefficients b_p in the Taylor expansion of the local truncation error e, we can show that $k_6=1/2$ and $k_4=-1/2$ (all other $k_i=0$, i=1,2,3,5,7,8,9) in Eq. (38) yield the optimal order of e in Eq. (39):

$$e = -\frac{h^3}{6} \frac{\partial^3 u_5}{\partial x^3} + O(h^4). \tag{40}$$

In this case we have the well-known finite-difference approximation of the derivative. In contrast to the third order of the local truncation error in Eq. (40), OLTEM provides the fourth order of the local truncation error for homogeneous materials and improves the accuracy of the spatial derivative of by one order for the same 9-point compact stencils. We should also mention that the approximation given by Eq. (38) cannot be used for the stencils with interfaces (as those in Figure 1b).

To summarize, the proposed post-processing procedure provides the optimal accuracy of the spatial derivatives of displacements calculated with the help of compact stencils. It can be developed with or without the use of PDEs. However, the use of PDEs improves the accuracy of the spatial derivatives for the given stencils. Despite the fact that we have applied the proposed post-processing technique to the stencils defined on Cartesian meshes, it can be also used for non-uniform meshes with the corresponding coefficients $r_{x,p}$, $r_{y,p}$ in Eq. (9) (similar to OLTEM developed in our papers [42, 44, 55] for irregular boundaries). Finally, the post-processing procedure developed can be independently used with any known numerical technique (e.g., with finite elements).

4. Numerical examples

In this section the computational efficiency of OLTEM with the 9-point stencils developed for the solution of the 2-D elastodynamics equations with discontinuous coefficients will be demonstrated and compared with conventional linear and high order (up to 5th order, the highest order in "COMSOL") triangular finite elements. For finite element calculations, the commercial finite element software "COMSOL" with isoparametric finite elements is used. In order to compare the accuracy of OLTEM with FEM, the following errors are considered below. The relative error e^j_w for the function w at the j^{th} grid point is defined as:

$$e_w^j = \frac{|w_j^{num} - w_j^{exact}|}{w_{\max}^{exact}}, \qquad j = 1, 2, ..., N.$$
 (41)

The maximum relative error e_w^{max} for the function w is defined as:

$$e_w^{\text{max}} = \max_j e_w^j, \qquad j = 1, 2, ..., N.$$
 (42)

In Eqs. (41) and (42) the superscripts "num" and "exact" correspond to the numerical and exact solutions, N is the total number of the grid points used in calculations, $w_{\text{max}}^{\text{exact}}$ is the maximum absolute value of the exact solution over the entire domain for the function w. We also use the relative error in the L^2 norm for finite elements (e.g., see [56]) and the relative error in the l^2 norm (e.g., see [57]) for OLTEM:

$$e_{w}^{l^{2}} = \left\{ dx \ dy \ \sum_{i=0}^{N_{x}} \sum_{j=0}^{N_{y}} \left[w^{num}(x_{i}, y_{j}, t) - w^{exact}(x_{i}, y_{j}, t) \right]^{2} \right\}^{\frac{1}{2}} /$$

$$|w^{exact}|_{L^{2}},$$
(43)

where N_x and N_y are the numbers of Cartesian grid points along x- and y-axes, x_i and y_j are the coordinates of Cartesian grid points, respectively. As function w in Eqs. (41)–(43) we consider the displacements u and v, the velocities $\dot{u} = \frac{du}{dt}$ and $\dot{v} = \frac{dv}{dt}$, as well as the stresses s_x , s_y and s_{xy} .

4.1. Test problem: a square plate with a circular interface

Let us consider a square plate *ABCD* with dimensions 2×2 ; see Figure 2. A circular interface with the radius $r_0 = \pi/8$ centered at the origin O(0, 0) divides the domain Ω into two subdomains: the circular subdomain Ω_I and the remaining subdomain Ω_{II} . For the circular interface, the components of the unit normal vector used in the interface conditions equal $n_x = \frac{x}{r_0}$ and $n_y = \frac{y}{r_0}$ for any interface point with the coordinate (x, y). Using the method of manufactured solutions, the following exact solution is selected:

$$\begin{cases} u_I(x,y,t) = \frac{(\sqrt{r^2+1})^{\alpha}}{\lambda_I} \sin{(\omega t)}, \\ v_I(x,y,t) = \frac{(\sqrt{r^2+1})^{\beta}}{\lambda_I} \sin{(\omega t)}, \end{cases} \text{ in } \Omega_I$$

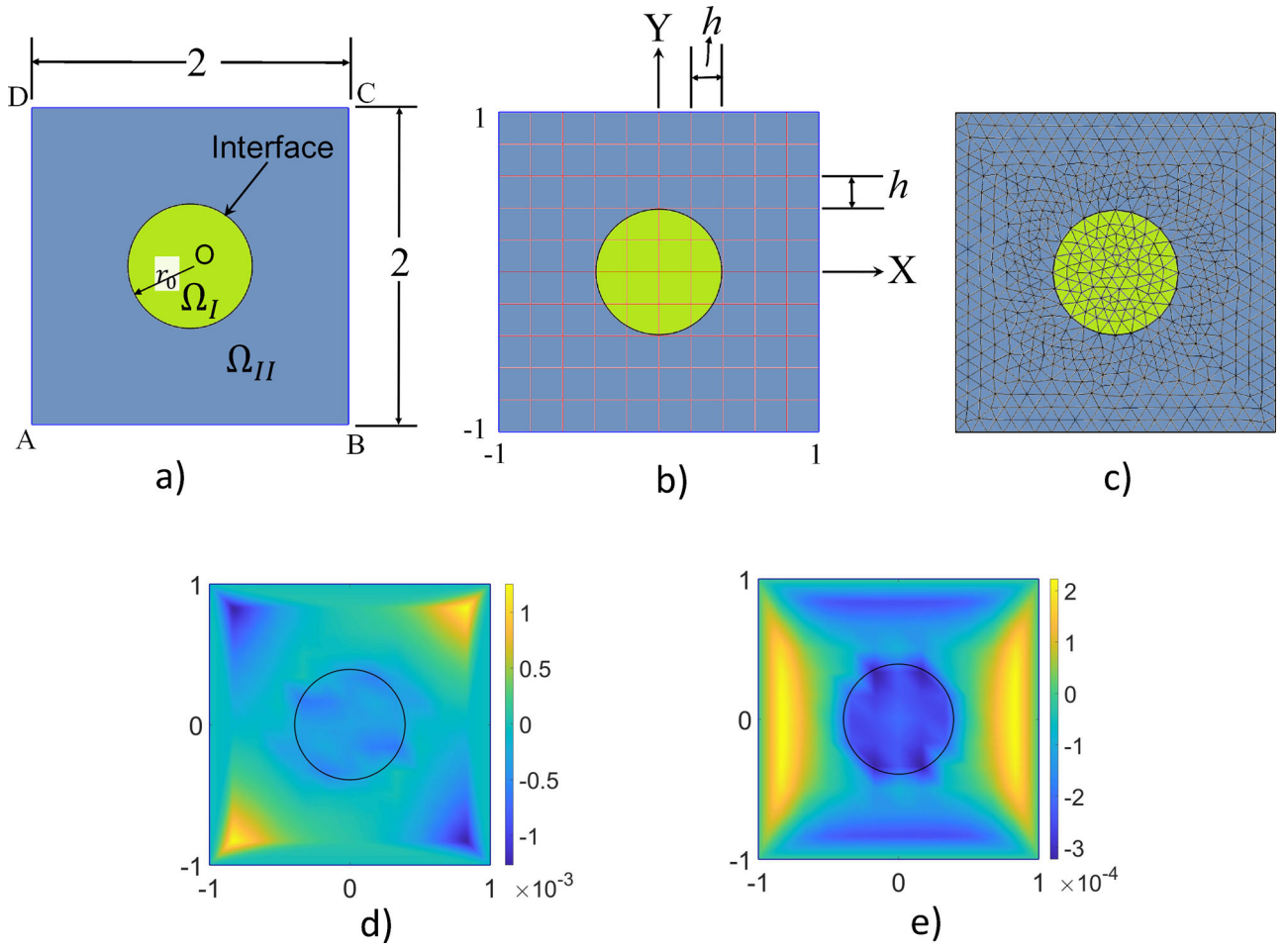


Figure 2. A square plate ABCD with a circular interface centered at O(0, 0) with the radius $r_0 = \pi/8$ (a). Examples of an unfitted square Cartesian mesh for OLTEM (b), of a conformed triangular finite element mesh (c) generated by COMSOL. The distribution of the relative errors in displacements e_u (d) and e_v (e) at the final time T = 0.2 obtained by OLTEM with the non-diagonal mass matrix on a square Cartesian mesh of size h = 1/6 (the material contrast $\frac{E_f}{E_f} = 2$).

$$\begin{cases} u_{II}(x,y,t) = \left[\frac{\left(\sqrt{r^2+1}\right)^{\alpha}}{\lambda_{II}} + \left(\frac{1}{\lambda_{I}} - \frac{1}{\lambda_{II}}\right) \left(\sqrt{r_0^2+1}\right)^{\alpha} \right] \sin\left(\omega t\right), \\ v_{II}(x,y,t) = \left[\frac{\left(\sqrt{r^2+1}\right)^{\beta}}{\lambda_{II}} + \left(\frac{1}{\lambda_{I}} - \frac{1}{\lambda_{II}}\right) \left(\sqrt{r_0^2+1}\right)^{\beta} \right] \sin\left(\omega t\right), \end{cases}$$
 in Ω_{II} (44)

where $\alpha = 7$, $\beta = 10$, $\omega = 5$ and $r = \sqrt{x^2 + y^2}$. The body forces can be calculated by the substitution of the exact solution into the elastodynamics equations Eq. (1). Six different combinations of the elastic Lame's coefficients λ and μ are considered: 1) $\lambda_I = 5$, $\lambda_{II} = \frac{5}{2}$, $\mu_I = 2$, $\mu_{II} = 1$; 2) $\lambda_I =$ 5, $\lambda_{II} = \frac{1}{2}$, $\mu_{I} = 2$, $\mu_{II} = \frac{1}{5}$; 3) $\lambda_{I} = 5$, $\lambda_{II} = \frac{1}{20}$, $\mu_{I} = 2$, $\mu_{II} = \frac{1}{50}$; 4) $\lambda_{I} = \frac{5}{2}$, $\lambda_{II} = 5$, $\mu_{I} = 1$, $\mu_{II} = 2$; 5) $\lambda_{I} = \frac{1}{2}$, $\lambda_{II} = \frac{1}{2}$ 5, $\mu_I = \frac{1}{5}$, $\mu_{II} = 2$; 6) $\lambda_I = \frac{1}{20}$, $\lambda_{II} = 5$, $\mu_I = \frac{1}{50}$, $\mu_{II} = 2$. They correspond to the same Poisson's ratio $\nu_I = \nu_{II} = \frac{5}{14} = 0.357$ and the following Young's moduli $E_I = \frac{38}{7}; \frac{38}{7}; \frac{38}{7}; \frac{38}{14}; \frac{38}{70};$ $\frac{38}{700}$, $E_{II} = \frac{38}{14}$; $\frac{38}{70}$; $\frac{38}{700}$; $\frac{38}{7}$; $\frac{38}{7}$; $\frac{38}{7}$ with the contrast for Young's moduli $E_c = \frac{E_I}{E_{II}} = 2$; 10; 100; $\frac{1}{2}$; $\frac{1}{10}$; $\frac{1}{100}$. The density is selected to be $\rho_I = 1$ and $\rho_{II} = 4$. The exact solution given by Eqs. (44) with the selected material properties meets the interface conditions, Eqs. (3) and (4). The final observation time is selected to be T = 0.2.

The test problem is solved by OLTEM on square $(b_y = 1)$ Cartesian meshes as well as by conventional linear and high-order (up to the fifth order which is the maximum order implemented in COMSOL) isoparametric finite elements; see Figure 2b for an example of an unfitted Cartesian mesh used with OLTEM and see Figure 2c for an example of a conformed triangular finite element mesh generated by COMSOL (the numerical results on triangular and quadrilateral finite element meshes for the problems considered below are similar at the same number of degrees of freedom). The Dirichlet boundary conditions are imposed along the edges of the square plate according to the exact solution given by Eq. (44).

For the time integration of the semi-discrete equations of OLTEM with the non-diagonal mass matrix, the implicit trapezoidal rule is used. For the time integration of the semi-discrete equations of OLTEM with the diagonal mass matrix we use the explicit central-difference method which does not require the solution of the global system of algebraic equations. For the both time-integration methods, small time increments at which the error in time is negligible compared to the error in space are used. In this case, the numerical results shown below present the spacediscretization errors. Because the main unknowns for the time-integration of the elastodynamics equations are the displacements and velocities, we show the accuracy of these variables for all numerical results.



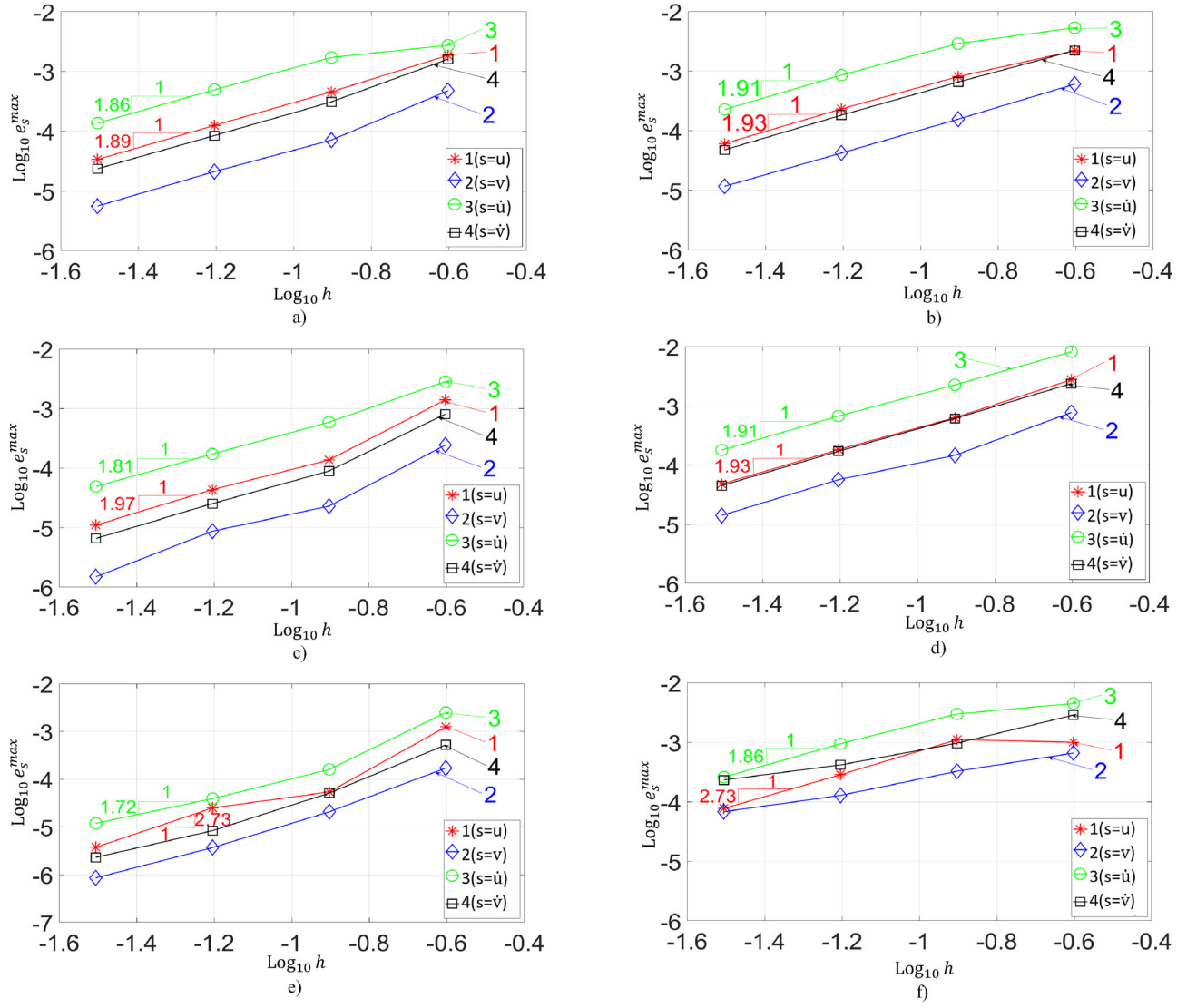


Figure 3. The maximum relative errors in displacements e_u^{\max} (curve 1) and e_v^{\max} (curve 2) as well as the maximum relative errors in velocities e_u^{\max} (curve 3) and e_{0}^{max} (curve 4) at the final time T=0.2 as a function of the mesh size h in the logarithmic scale. The numerical solutions for the test problem with the circular inter-Face are obtained by OLTEM with the non-diagonal mass matrix on square Cartesian meshes (see Figure 2b) with the following material contrasts: $\frac{E_l}{E_{ll}} = 2$ (a), $\frac{E_l}{E_{ll}} = \frac{1}{2}$ (b), $\frac{E_l}{E_{ll}} = 10$ (c), $\frac{E_l}{E_{ll}} = \frac{1}{10}$ (d), $\frac{E_l}{E_{ll}} = 100$ (e) and $\frac{E_l}{E_{ll}} = \frac{1}{100}$ (f).

The accuracy (errors) of the numerical results presented below will be analyzed and compared at the final observation time T = 0.2.

4.2. OLTEM with non-diagonal mass matrix. Test problem with different material contrasts $E_c = \frac{E_I}{E_B}$

Here, we present the convergence of OLTEM with the non-diagonal mass matrix for the test problem with heterogeneous materials described in Section 4.1. The six combinations of the material properties with the contrast in Young's moduli $E_c = \frac{E_I}{E_{II}} = 2; 10; 100; \frac{1}{2}; \frac{1}{10}; \frac{1}{100}$ are considered (see Section 4.1). Figures 3 and 4 show the maximum relative errors and the relatives errors in the l² norm for the displacements and velocities at the final time T = 0.2 at mesh refinement in the logarithmic scale. The slopes of the curves in these figures at the small mesh size h correspond to the order of convergence of OLTEM. Because the less accurate x- or y- component of the displacement (velocity) defines

the order of convergence of the displacement (velocity) vector, the slope of the curves in Figures 3 and 4 is designated for this component. As can be seen from the presented results, the order of convergence of OLTEM in the considered error norms is close to 2 for the displacements and velocities for the different materials contrasts. These observations are in agreement with the theoretical results in Section 2.

4.3. OLTEM with non-diagonal mass matrix. Comparison with FEM. Test problem with material contrast $\frac{E_i}{E_n} = 2$

In the all following sections, we analyze OLTEM for the test problem with the material contrast $E_c = \frac{E_I}{E_B} = 2$ in more detail (similar results can be obtained for other material contrasts). Figure 2d,e presents the distribution of the relative errors in displacements e_u (d) and e_v (e) at the final time T = 0.2 obtained by OLTEM with the non-diagonal mass matrix on a square Cartesian mesh of size h = 1/6. As

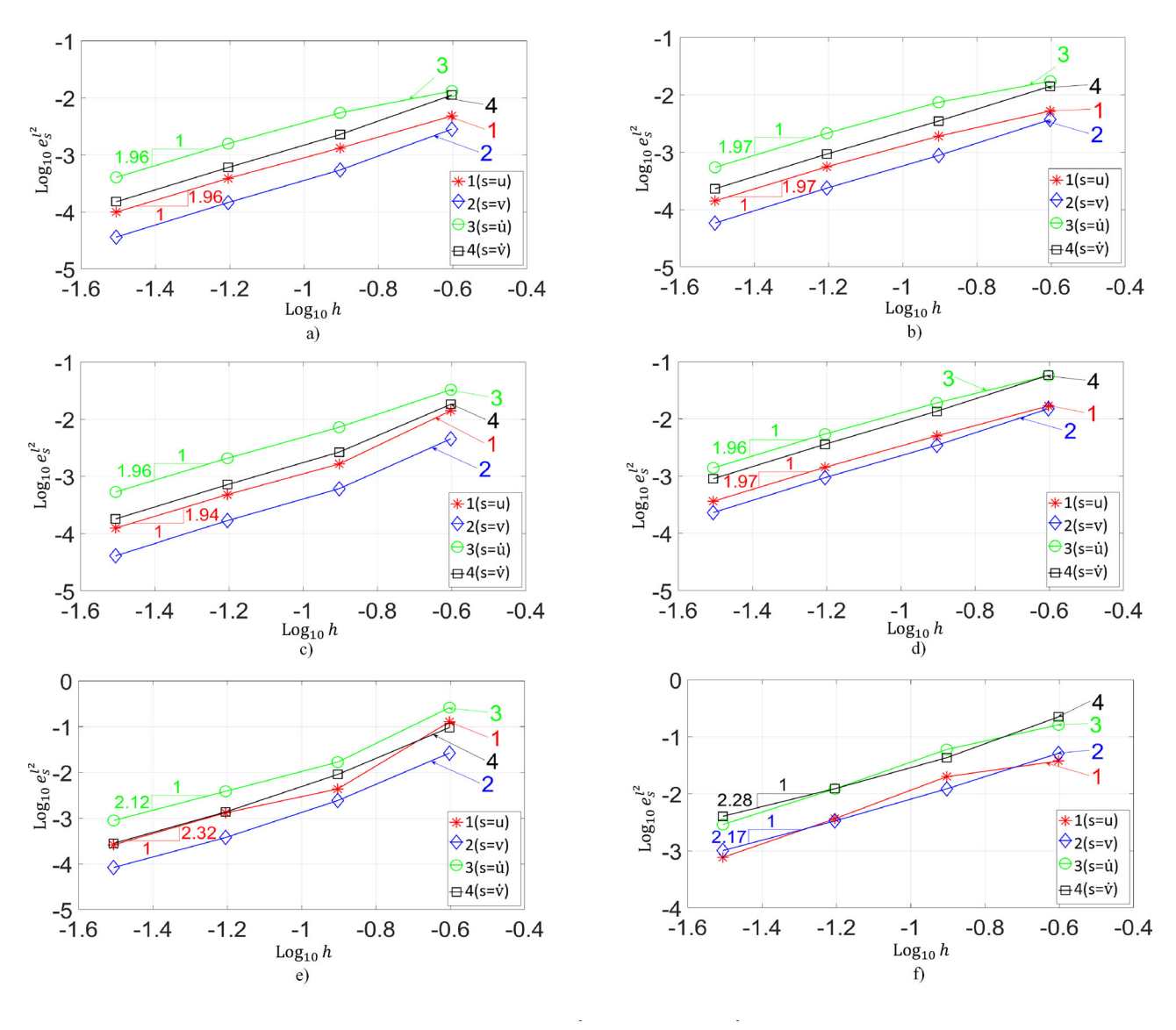


Figure 4. The relative errors in the l^2 norm for displacements e_{ν}^{l} (curve 1) and e_{ν}^{l} (curve 2) as well as the relative errors in the l^2 norm for velocities e_{ν}^{l} (curve 3) and e_{ν}^{l} (curve 4) at the final time T=0.2 as a function of the mesh size h in the logarithmic scale. The numerical solutions for the test problem with the circular interface are obtained by OLTEM with the non-diagonal mass matrix on square Cartesian meshes (see Figure 2b) with the following material contrasts: $\frac{E_1}{E_0}=2$ (a), $\frac{E_2}{E_1}=\frac{1}{10}$ (c), $\frac{E_1}{E_1}=\frac{1}{10}$ (d), $\frac{E_2}{E_1}=\frac{1}{10}$ (e) and $\frac{E_1}{E_1}=\frac{1}{100}$ (f).

can be seen from Figure 2d,e the results obtained by OLTEM are accurate (the errors are small). In order to compare the accuracy of the numerical solutions obtained by OLTEM and by conventional finite elements, Figure 5 shows the maximum relative errors e_u^{max} (a), e_v^{max} (b), and the relative errors $e_u^{L^2}$ (c), $e_v^{L^2}$ (d) in the L^2 norm for the displacements as a function of the number N of degrees of freedom in the logarithmic scale. As can be seen from Figure 5, at the same N the numerical results obtained by OLTEM are much more accurate than those obtained by linear finite elements; compare curves 1 and 2. At the engineering accuracy of 0.1% (-3 along the y-axis in Figure 5 corresponds to the error of 0.1%) for the u displacement in Figure 5c, OLTEM with the computational costs of linear finite elements reduces the number N of degrees of freedom by a factor of greater than 21 compared to that for linear finite elements. For the other displacements and the other error norms presented in Figure 5, the reduction in the number N of degrees of freedom for OLTEM at the engineering accuracy of 0.1% is even greater. This will lead to a significant reduction in the computation time for OLTEM compared to linear finite elements at a given accuracy. Moreover, OLTEM yields more accurate results for the displacements than those obtained by quadratic finite elements and by cubic (up to the accuracy of 0.1%) finite elements at the same number N; see curve 1 and curves 3,4 in Figure 5. This increase in accuracy by OLTEM is impressive considering the fact that higher order finite elements have much wider stencils compared to those for OLTEM (the width of the stencils for OLTEM corresponds to that for linear finite elements) and require a much greater computation time. Similar to Figure 5, the comparison of the numerical results for the velocities obtained by OLTEM and by linear and high-order finite elements is shown in Figure 6. Compared to FEM, the

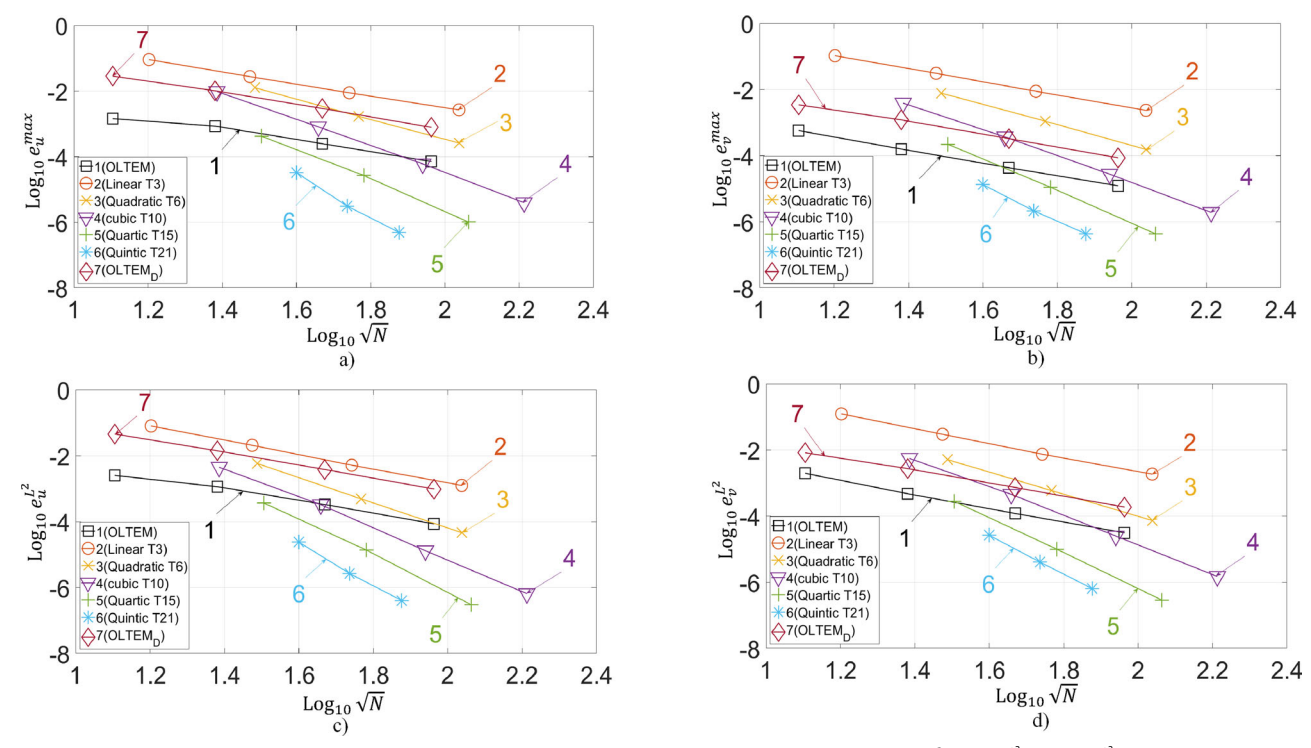


Figure 5. The maximum relative errors in displacements e_u^{max} (a) and e_v^{max} (b) as well as the relative errors in the L^2 norm $e_u^{L^2}$ (c) and $e_v^{L^2}$ (d) at the final time T=0.2 as a function of the number N of degrees of freedom in the logarithmic scale. The test problem with the material contrast $\frac{E_L}{E_V}=2$ was solved by OLTEM on unfitted square Cartesian meshes and by FEM on triangular meshes. Curves 1 and 7 correspond to OLTEM with the non-diagonal and diagonal mass matrices, respectively. Curves 2,3,4,5,6 correspond to linear, quadratic, cubic, 4-th order and 5-th order finite elements, respectively.

advantages in accuracy of OLTEM for the velocities in Figure 6 are similar to those in Figure 5 for the displacements; see curve 1 and curves 2,3,4 in Figure 6.

Next, we compare the accuracy of stresses s_x , s_y and s_{xy} obtained by OLTEM with the new post-processing procedure described in Section 3 and obtained by linear and high order finite elements that are shown in Figure 7. Similar to the displacements and velocities in Figures 5 and 6, the maximum relative errors $e_{s_x}^{\text{max}}$ (a), $e_{s_y}^{\text{max}}$ (c), $e_{s_x y}^{\text{max}}$ (e) as well as the relative errors in the L^2 norm $e_{s_x}^{L^2}$ (b), $e_{s_v}^{L^2}$ (d) and $e_{s_xy}^{L^2}$ (f) are plotted as a function of the number N of degrees of freedom. As can be seen from Figure 7, at the same N the stresses obtained by OLTEM are much more accurate than those obtained by linear finite elements; compare curves 1 with curves 2. At the engineering accuracy of 0.1%, for the all stresses components and considered error norms, OLTEM reduces the number N of degrees of freedom by a factor of greater than 12.5. 10³ compared to that for linear finite elements; compare curves 1 with curves 2 in Figure 7. This will lead to a huge reduction in the computation time for OLTEM compared to linear finite elements at a given accuracy. Moreover, OLTEM yields more accurate results for the stresses than those obtained by quadratic and cubic finite elements as well as by the fourth order (up to the accuracy of 0.1%) finite elements at the same number N; see curve 1 and curves 3,4,5 in Figure 5. It is also interesting to note that due to the new post-processing procedure for the stress calculations, the difference in accuracy between OLTEM and FEM is greater for the stresses (see Figure 7) compared to that for the displacements and velocities (see Figures 5 and 6). This is very important for the problems where the accurate calculations of stresses are crucial for accurate predictions (e.g., simulations of crack propagation).

In order to study the convergence and stability of the numerical results obtained by OLTEM in more detail, Figure 8 presents the curves 1-4 in Figures 3a and 4a at small changes of the mesh size h. We solve the test problem on 1001 Cartesian meshes with the mesh sizes $h_i =$ $h_1 + \frac{(h_2 - h_1)(i-1)}{1000}$ where $h_1 = 1/4 = 0.25$, $h_2 = 1/16 = 0.0625$ and i = 1, 2, ..., 1001. For these meshes, two grid lines always coincide with the left and bottom lines of the square domain; see Figure 2b. At the small variations of the mesh size h we have very different locations of the circular interface with respect to the grid points. As can be seen from Figure 8, the numerical results obtained by OLTEM converge with the decrease in the grid size h. The oscillatory behavior can be explained by the fact that at small variations of the mesh size h, there is a discontinuous change in the location of the grid points with respect to the interface (e.g., some grid points that belong to one material for the previous mesh can belong to another material for the next mesh; this leads to the discontinuous change of some stencils equations for the meshes with a small difference in h). It is important to mention that small oscillations in numerical convergence curves are typical for many numerical techniques at small variations of h. For example, the change in the

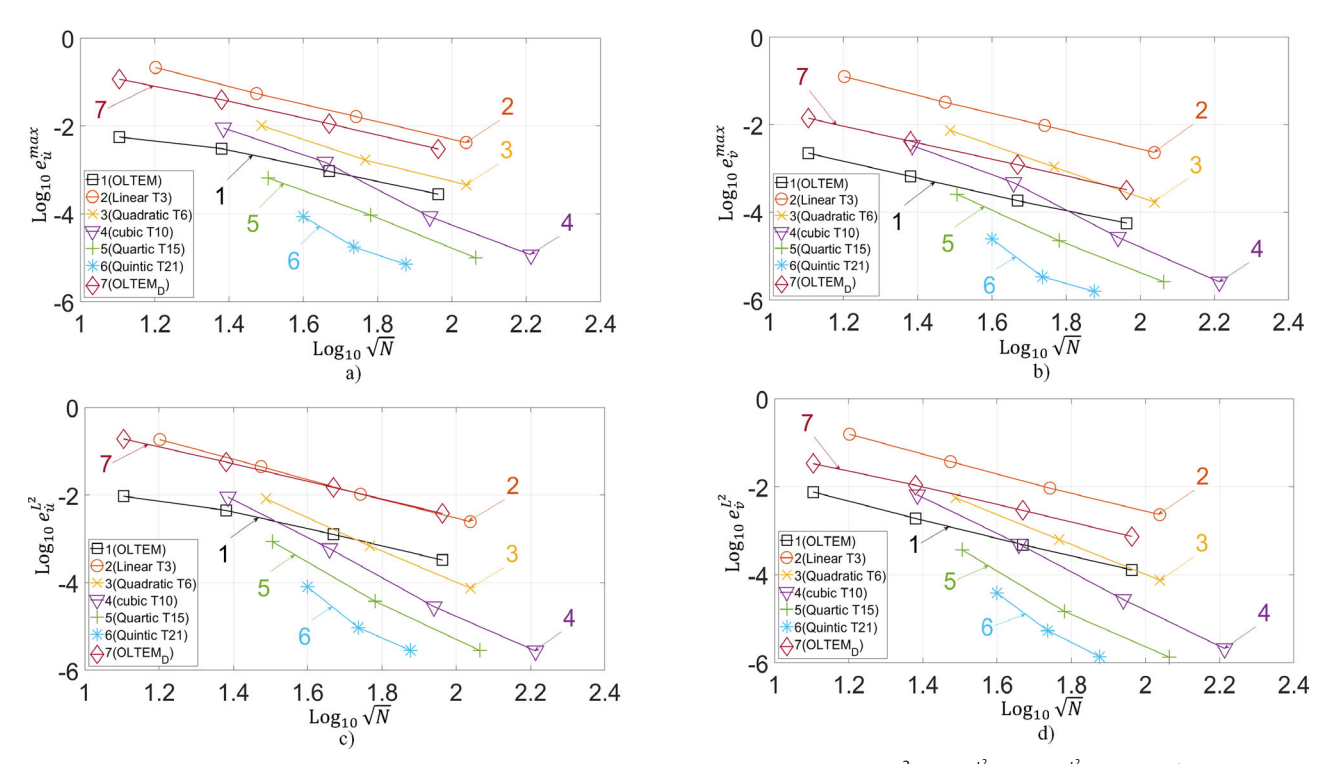


Figure 6. The maximum relative errors in velocities $e_{\tilde{u}}^{\max}$ (a) and $e_{\tilde{v}}^{\max}$ (b) as well as the relative errors in the L^2 norm $e_{\tilde{v}}^{L^2}$ (c) and $e_{\tilde{v}}^{L^2}$ (d) at the final time T=0.2 as a function of the number N of degrees of freedom in the logarithmic scale. The test problem with the material contrast $\frac{E_L}{E_L}=2$ was solved by OLTEM with the non-diagonal mass matrix on unfitted square Cartesian meshes and by FEM on conformed triangular meshes. Curves 1 and $\frac{E_L}{I}$ correspond to OLTEM with the non-diagonal and diagonal mass matrices, respectively. Curves 2,3,4,5,6 correspond to linear, quadratic, cubic, 4-th order and 5-th order finite elements, respectively.

angles of finite elements at small variations of the element size h also leads to such oscillations in convergence curves for finite element techniques.

4.4. OLTEM with diagonal mass matrix. Test problem with material contrast $\frac{E_1}{E_n} = 2$

As we mentioned in the beginning of this section, the explicit central difference time-integration method is used for OLTEM with the diagonal mass matrix. This allows to avoid the solution of the global system of algebraic equations at time integration; however, this imposes the restriction on the size of time increments (it should be smaller than the stability limit). To study the effect of the size Δt of time increments on the accuracy of OLTEM, Figure 9 shows the maximum relative errors for the displacements at the final time T = 0.2 as a function of Δt on an unfitted Cartesian mesh with 2178 degrees of freedom. The stability limit for this mesh is close to $\Delta t^{st} \approx 11.2 \cdot 10^{-3}$. For $\Delta t > \Delta t^{st}$, the accuracy of the results obtained by OLTEM explosively decreases. It is interesting to mention that the decrease in the size of time increments below the stability limit Δt < Δt^{st} does not practically effect the accuracy of the numerical results obtained by OLTEM; see Figure 9.

Unfortunately, the diagonal mass matrix is not implemented in COMSOL. Therefore, below we compare OLTEM with the diagonal mass matrix and the numerical results obtained by OLTEM and FEM with the non-diagonal mass matrices. Similar to curves 1 and 2 in Figure 9, curves 3 and 4 in Figure 9 show the accuracy of the numerical results for the displacements obtained by linear triangular finite

elements with the non-diagonal mass matrix and 10466 degrees of freedom. For the selected meshes, OLTEM and linear finite elements provide approximately the same accuracy in space for the displacement u at small Δt (see curves 1 and 3). Curves 3 and 4 also shows that for the accurate results, the size of time increments used by linear finite elements with the implicit time-integration method should be close to the stability limit $\Delta t^{st} \approx 11.2 \cdot 10^{-3}$ for OLTEM with the diagonal mass matrix and the explicit time-integration method.

Next, the accuracy of OLTEM with the diagonal mass matrix and FEM are compared at mesh refinement. As can be seen from Figures 5 and 6, at the same N the numerical results for the displacements and velocities obtained by OLTEM with the diagonal mass matrix are less accurate than those obtained by OLTEM with the non-diagonal mass matrix; see curves 1 and 7. This can be explained by the fact that the 9-point stencils with the diagonal mass matrix include a smaller number 17 of the stencils coefficients for the diagonal mass matrix compared to the 36 stencils coefficients for the non-diagonal mass matrix (see Eq. 12) used for the minimization of the local truncation error in Eq. (24). Nevertheless, OLTEM with the diagonal mass matrix yields more accurate results for the displacements and velocities than those for linear finite elements; see curves 2 and 7 in Figures 5 and 6.

Let us analyze the accuracy of the stresses obtained by OLTEM with the diagonal mass matrix and the new post-processing procedure. Because, the stress calculation does not include the solution of the global system of algebraic equations, for post-processing we use 9-point stencils with

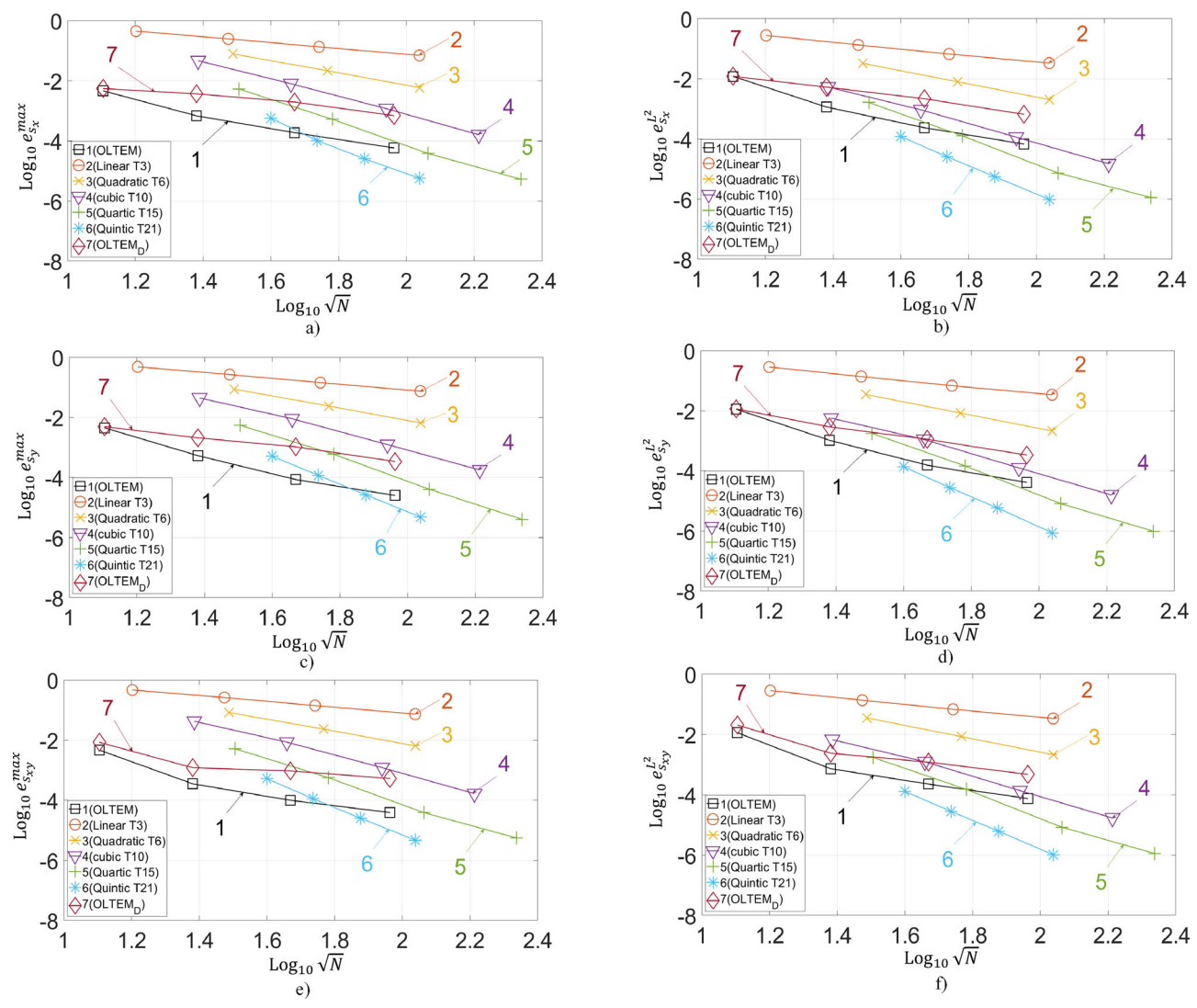


Figure 7. The maximum relative errors in stresses $e_{s_x}^{\text{max}}$ (a), $e_{s_y}^{\text{max}}$ (c), $e_{s_y}^{\text{max}}$ (e) as well as the relative errors in stresses in the L^2 norm $e_{s_x}^{L^2}$ (b), $e_{s_y}^{L^2}$ (d), $e_{s_y}^{L^2}$ (f) at the final time T=0.2 as a function of the number N of degrees of freedom in the logarithmic scale. The test problem with the material contrast $\frac{E_I}{E_{IJ}}=2$ was solved by OLTEM on unfitted square Cartesian meshes and by FEM on conformed triangular meshes. Curves 1 and 7 correspond to OLTEM with the non-diagonal and diagonal mass matrices, respectively. Curves 2,3,4,5,6 correspond to linear, quadratic, cubic, 4-th order and 5-th order finite elements, respectively.

36 stencil coefficients (see Eq. 31) along with the displacements and accelerations obtained by OLTEM with the diagonal mass matrix in basic computations. Similar to the displacements and velocities, at the same N the numerical results for the stresses obtained by OLTEM with the diagonal mass matrix are less accurate than those obtained by OLTEM with the non-diagonal mass matrix; see curves 1 and 7 in Figure 7. Nevertheless, at the same N the stresses obtained by OLTEM with the diagonal mass matrix are much more accurate than those obtained by linear finite elements; compare curves 7 with curves 2. At the engineering accuracy of 0.1%, for the all stress components and the considered error norms, OLTEM with the diagonal mass matrix reduces the number N of degrees of freedom by a factor of greater than $3.1 \cdot 10^3$ compared to that for linear finite elements; compare curves 7 with curves 2 in Figure 7. This will lead to a huge reduction in the computation time for OLTEM compared to linear finite elements at a given accuracy. Moreover, OLTEM with the diagonal mass matrix yields even more accurate results for the stresses than those obtained by quadratic finite elements as well as by cubic (up to the accuracy of 0.1%) finite elements at the same number N; see curve 1 and curves 3,4 in Figure 5. It is also interesting to note that due to the new post-processing procedure for the stress calculations, the difference in accuracy between OLTEM and FEM is greater for the stresses (see Figure 7) compared to that for the displacements and velocities (see Figures 5 and 6). This is very important for the problems where the accurate calculations of stresses are crucial for accurate predictions (e.g., simulations of crack propagation). We should also mention that in contrast to OLTEM with the diagonal mass matrix, the finite element results in Figures 5-7 include the solution of the global system of algebraic equations that leads to the additional computa-

Similar to Figure 8 for OLTEM with the non-diagonal mass matrix, Figure 10 shows the convergence and stability of OLTEM with the diagonal mass matrix on 1001 meshes with very small variations of the mesh size h (see also the corresponding text in Section 4.3).

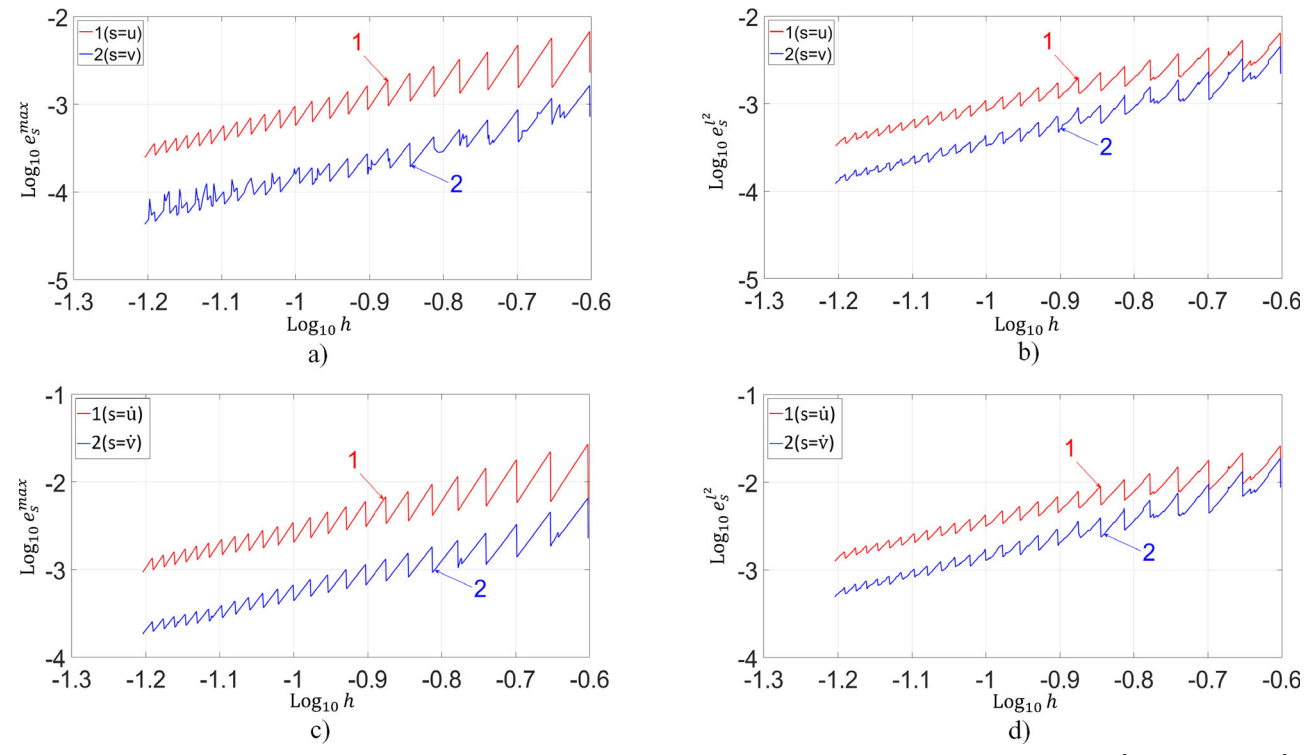


Figure 8. The maximum relative errors in displacements e_u^{\max} (curve 1 in (a)), e_v^{\max} (curve 2 in (a)) and the relative errors in the l^2 norm e_u^l (curve 1 in (b)), e_v^{μ} (curve 2 in (b)) as well as the maximum relative errors in velocities e_u^{\max} (curve 1 in (c)), e_v^{\max} (curve 2 in (c)) and the errors in the l^2 norm e_u^l (curve 1 in (d)), e_v^l (curve 2 in(d)) at the final time T=0.2 as a function of the mesh size e_u^l in the logarithmic scale. The test problem with the material contrast $\frac{E_l}{E_l}=2$ was solved by OLTEM with the non-diagonal mass matrix on 1001 unfitted square Cartesian meshes.

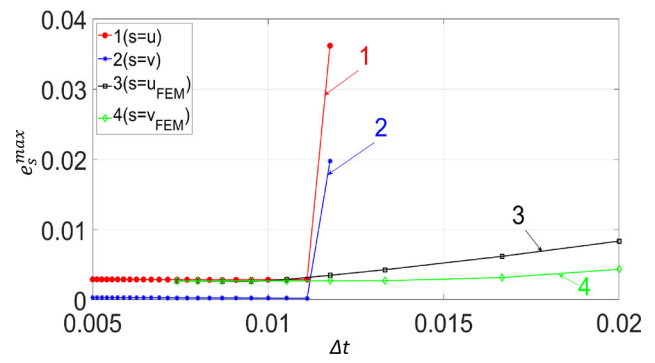


Figure 9. The maximum relative errors in displacements e_u^{max} (curves 1 and 3) and e_v^{max} (curves 2 and 4) at the final time T=0.2 as a function of the size of time increments Δt . The numerical solutions for the test problem with the material contrast of $\frac{E_1}{E_3}=2$ are obtained by OLTEM with the diagonal mass matrix on a square Cartesian mesh with 2178 degrees of freedom (curves 1 and 2) and by linear triangular finite elements with the non-diagonal mass matrix and 10466 degrees of freedom (curves 3 and 4).

5. Concluding remarks

OLTEM developed in our paper [51] for the scalar wave equation with heterogeneous materials is here extended to a more complex case of a system of the time-dependent PDEs related to elastodynamics. 9-point stencils (similar to those for linear finite elements) and unfitted Cartesian meshes for irregular geometry are used. One of the main ideas of the proposed approach for heterogeneous materials with interfaces is the addition of the interface conditions at a small number of interface points to the expression for the local truncation error of the stencil equations. The calculation of the unknown stencil coefficients is based on the

minimization of the local truncation error of the stencil equations and yields the optimal second order of accuracy of the new technique at a given stencil width. Finally, the unknown stencil coefficients are numerically calculated from a small local system of algebraic equations for general geometry of interfaces. OLTEM does not change the width of the stencil equations for heterogeneous materials; i.e., the size of the global semi-discrete system of equations is the same for the elastodynamics equations with constant or discontinuous coefficients. The increase in the computational costs for the calculation of the unknown stencil coefficients from the local system is insignificant compared to the computational costs for the solution of the global semi-discrete system. The extension of OLTEM from the scalar wave equation to a system of the elastodynamics equations is not trivial due to the increase in the number of stencil coefficients for elastodynamics (by a factor of two compared to the scalar wave equation) and some analytical expressions for the local truncation error that may become intractable. In contrast to our paper [51] for the scalar wave equation, here we have proposed a new approach for the calculation of the right-hand side of the stencil equations due to body forces that significantly simplifies the analytical derivations of OLTEM for time-dependent problems. In this article, for the first time we have also developed OLTEM with the diagonal mass matrix for time-dependent problems. In contrast to many known approaches with some ad-hoc procedures for the calculation of the diagonal mass matrix (e.g., "row summation" and other techniques; see [5, 6, 8]), OLTEM offers a rigorous approach. The calculation of the diagonal mass matrix in OLTEM is a particular case of the more general non-

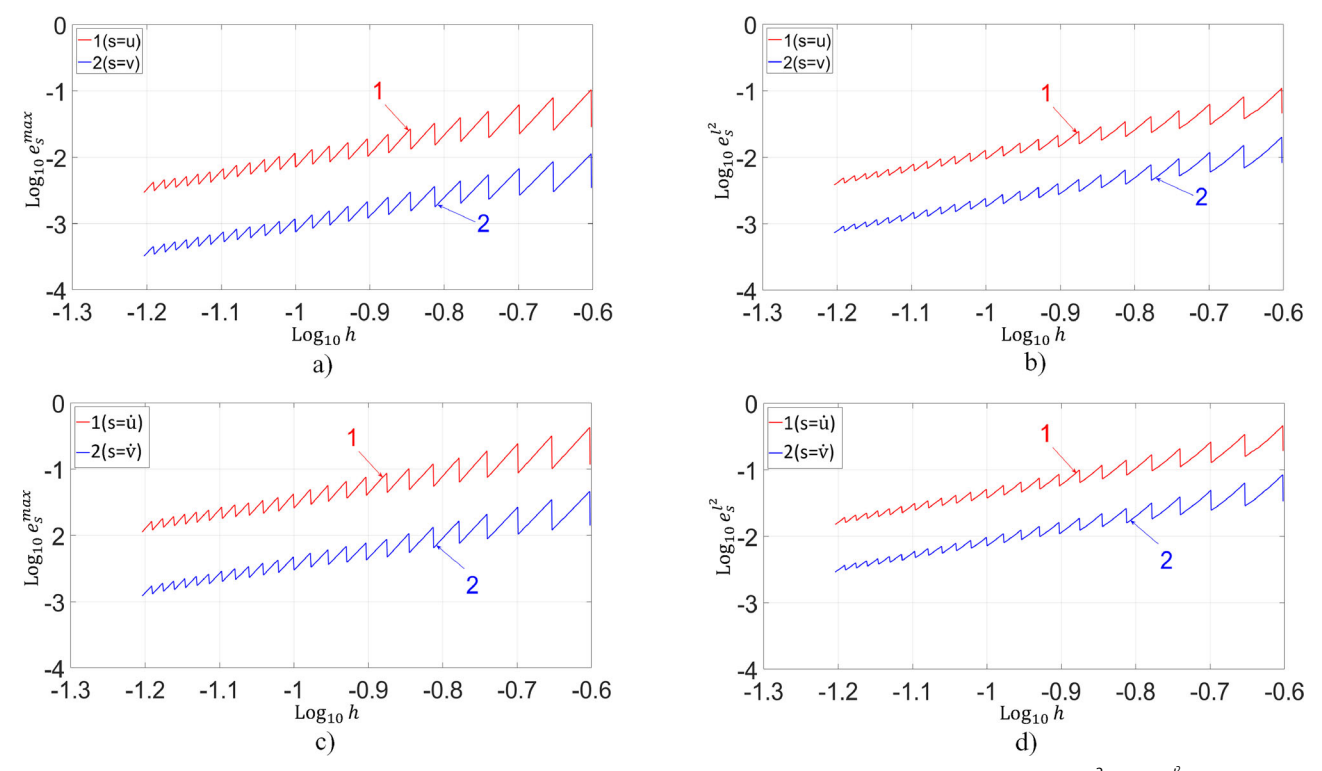


Figure 10. The maximum relative errors in displacements e_u^{\max} (curve 1 in (a)), e_v^{\max} (curve 2 in (a)) and the relative errors in the l^2 norm $e_u^{l^2}$ (curve 1 in (b)), $e_v^{l^2}$ (curve 2 in (b)) as well as the maximum relative errors in velocities e_u^{\max} (curve 1 in (c)), e_v^{\max} (curve 2 in (c)) and the errors in the l^2 norm $e_u^{l^2}$ (curve 1 in (d)), $e_v^{l^2}$ (curve 2 in(d)) at the final time l^2 norm l^2 as a function of the mesh size l^2 in the logarithmic scale. The test problem with the material contrast l^2 in (b), l^2 as solved by OLTEM with the diagonal mass matrix on 1001 unfitted square Cartesian meshes.

diagonal mass matrix when the non-diagonal stencil coefficients of the mass matrix are assumed to be zero.

Another novelty of the article is the development of a new post-processing procedure for the accurate calculations of stresses. The proposed post-processing technique includes the same compact 9-point stencils as those in basic computations, the use of the partial differential equations and the solution of the small local systems of algebraic equations similar to those used for the calculations of the stencils coefficients in basic computations. It is also interesting to note that in contrast to known finite element and other post-processing techniques, OLTEM uses the accelerations along with the displacements at the grid points for the stress calculations.

The main advantages of the suggested technique can be summarized as follows:

- Many difficulties of the existing numerical techniques for irregular domains (e.g., finite elements, spectral element, isogeometric elements, the finite volume method, and many other) are related to complicated mesh generators for conformed meshes and the poor accuracy of "bad" elements (e.g., the elements with small angles) especially for elastodynamics problems. In contrast to these techniques, OLTEM is based on trivial unfitted Cartesian meshes with the trivial procedure for the formation of the 9-point stencils for 2-D domains with complex irregular interfaces.
- The new approach has the same width of the stencil equations and the same structure of the sparse global semi-discrete equations for the elastodynamics equations with constant and discontinuous coefficients. There are no

- unknowns on the interfaces between different materials for the proposed technique; i.e., complex irregular interfaces do not affect the structure of the global system of equations (they affect just the values of the stencils coefficients).
- OLTEM does not require the time consuming numerical integration for finding the coefficients of the stencil equations; e.g., as for high-order finite, spectral and isogeometric elements. The stencil coefficients are calculated analytically or numerically (for the general geometry of interfaces) by the solution of small local systems of linear algebraic equations. Numerical experiments show that the solution of these small local systems of algebraic equations is fast. Moreover, these local systems are independent of each other and can be efficiently solved on a parallel computer.
- The numerical results for an irregular interface show that at the same number of degrees of freedom, OLTEM with the non-diagonal mass matrix on unfitted meshes yields even much more accurate results for the displacements and velocities than those for linear as well as quadratic and cubic (with much wider stencils) finite elements with the nondiagonal mass matrix on conformed meshes. This also means that at a given accuracy, OLTEM significantly reduces the computation time compared to that for linear, quadratic and cubic finite elements. For example, at accuracy of 0.1% OLTEM decreases the number of degrees of freedom by a factor of greater than 21 compared to linear finite elements with similar stencils and conformed meshes.
- The numerical results for an irregular interface also show that at the same number of degrees of freedom, OLTEM



with the diagonal mass matrix on unfitted meshes yields slightly more accurate results for the displacements and velocities than those for linear finite elements with the non-diagonal mass matrix on conformed meshes. However, OLTEM with the diagonal mass matrix is used with the explicit time-integration method and does not require the solution of the global system of algebraic equations.

- It was shown that OLTEM with the 9-point compact stencils used for basic computations can be also applied (with small modifications) to the calculation of stresses at post-processing. The proposed post-processing procedure includes the use of the elastodynamics partial differential equations and the solutions of small local systems of algebraic equations. Numerical experiments show that OLTEM with the non-diagonal mass matrix and 9-point stencils used for basic computations and post-processing yields much more accurate results for stresses compared to linear and high-order (up to the 4-th order) finite elements with much wider stencils. At the engineering accuracy of 0.1% for stresses, OLTEM with the non-diagonal mass matrix decreases the number of degrees of freedom by a factor of greater than 10⁴ compared to linear finite elements. This is very important for the problems where accurate calculations of stresses are critical (e.g., for crack propagation in fracture mechanics).
- The proposed post-processing procedure for the stress calculation based on OLTEM with the non-diagonal mass matrix can be also applied to the numerical results obtained by OLTEM with the diagonal mass matrix because the post-processing procedure does not require the solution of the global system of algebraic equations. In this case basic computations with OLTEM and the diagonal mass yield the stresses that are more accurate than those obtained by linear and high-order (up to the 3-rd order) finite elements with much wider stencils and the non-diagonal mass matrix. At the engineering accuracy of 0.1% for stresses, OLTEM with the diagonal mass matrix decreases the number of degrees of freedom by a factor of greater than $3 \cdot 10^3$ compared to linear finite elements with the non-diagonal mass matrix.
- Despite the fact that we have applied the post-processing procedure to the stencils defined on Cartesian meshes, it can be equally used for non-uniform meshes (similar to OLTEM developed in our papers [42, 44, 55] for irregular boundaries). Finally, the post-processing procedure developed can be independently used with any known numerical technique (e.g., with finite elements).

In the future we plan to develop OLTEM with adaptive mesh refinement similar to h- and p- mesh refinement for finite elements (e.g., it was shown in papers [46, 48] that OLTEM can easily combine different stencils). We plan to use quadtrees/octrees meshes that allow a simple refinement strategy with Cartesian meshes. The extension of OLTEM to other PDEs with discontinuous coefficients as well as to non-linear PDEs will be also considered in the future. We plan to extend the new post-processing procedure with OLTEM to other PDEs.

Acknowledgments

The views and conclusions contained in this article are those of the authors and should not be interpreted as representing the official policies.

Funding

The research has been supported in part by the Army Research Office (Grant Number W911NF-21-1-0267), the NSF grant CMMI-1935452 and by Texas Tech University.

References

- K. Duru, L. Rannabauer, A.-A. Gabriel, O. K. A. Ling, H. Igel, and M. Bader, A stable discontinuous galerkin method for linear elastodynamics in 3d geometrically complex elastic solids using physics based numerical fluxes, Comput. Method. Appl. Mech. Eng., vol. 389, pp. 114386, 2022. DOI: 10.1016/j.cma. 2021.114386.
- J. Wang, and M. C. Hillman, Temporal stability of collocation, Petrov-Galerkin, and other non-symmetric methods in elastodynamics and an energy conserving time integration, Comput. Method. Appl. Mech. Eng., vol. 393, pp. 114738, 2022. DOI: 10. 1016/j.cma.2022.114738.
- M. Almquist, and E. M. Dunham, Elastic wave propagation in anisotropic solids using energy-stable finite differences with weakly enforced boundary and interface conditions, J Comput Phys., vol. 424, pp. 109842, 2021. DOI: 10.1016/j.jcp.2020.109842.
- M. A. Bhouri, and A. T. Patera, A two-level parameterized model-order reduction approach for time-domain elastodynamics, Comput. Method. Appl. Mech. Eng., vol. 385, pp. 114004, 2021. DOI: 10.1016/j.cma.2021.114004.
- J. Zhang, A. Ankit, H. Gravenkamp, S. Eisentrager and C. Song, A massively parallel explicit solver for elasto-dynamic problems exploiting octree meshes, Comput. Method. Appl. Mech. Eng., vol. 380, pp. 113811, 2021.
- M. A. Sanchez, B. Cockburn, N.-C. Nguyen, and J. Peraire, Symplectic hamiltonian finite element methods for linear elastodynamics, Comput. Method. Appl. Mech. Eng., vol. 381, pp. 113843, 2021. DOI: 10.1016/j.cma.2021.113843.
- H. Gravenkamp, C. Song, and J. Zhang, On mass lumping and explicit dynamics in the scaled boundary finite element method, Comput. Method. Appl. Mech. Eng., vol. 370, pp. 113274, 2020. DOI: 10.1016/j.cma.2020.113274.
- C. Anitescu, C. Nguyen, T. Rabczuk, and X. Zhuang, Isogeometric analysis for explicit elastodynamics using a dualbasis diagonal mass formulation, Comput. Method. Appl. Mech. Eng., vol. 346, pp. 574-591, 2019. DOI: 10.1016/j.cma. 2018.12.002.
- K. Park, H. Chi, and G. H. Paulino, On nonconvex meshes for elastodynamics using virtual element methods with explicit time integration, Comput. Method. Appl. Mech. Eng., vol. 356, pp. 669-684, 2019. DOI: 10.1016/j.cma.2019.06.031.
- K. Singh, and J. Williams, A parallel fictitious domain multigrid preconditioner for the solution of Poisson's equation in complex geometries, Comput. Method. Appl. Mech. Eng., vol. 194, no. 45-47, pp. 4845-4860, 2005. DOI: 10.1016/j.cma.2005.01.003.
- P. Vos, R. van Loon, and S. Sherwin, A comparison of fictitious domain methods appropriate for spectral/hp element discretisations, Comput. Method. Appl. Mech. Eng., vol. 197, no. 25-28, pp. 2275-2289, 2008. DOI: 10.1016/j.cma.2007.11.023.
- [12] E. Burman, and P. Hansbo, Fictitious domain finite element methods using cut elements: I. A stabilized lagrange multiplier

- method, Comput. Method. Appl. Mech. Eng., vol. 199, no. 41-44, pp. 2680-2686, 2010. DOI: 10.1016/j.cma.2010.05.011.
- E. Rank, S. Kollmannsberger, C. Sorger, and A. Duster, Shell finite cell method: A high order fictitious domain approach for thinwalled structures, Comput. Method. Appl. Mech. Eng., vol. 200, no. 45–46, pp. 3200–3209, 2011. DOI: 10.1016/j.cma.2011.06.005.
- [14] E. Rank, M. Ruess, S. Kollmannsberger, D. Schillinger, and A. Duster, Geometric modeling, isogeometric analysis and the finite cell method, Comput. Method. Appl. Mech. Eng., vol. 249-252, pp. 104-115, 2012. DOI: 10.1016/j.cma.2012.05.022.
- T. Fries, S. Omerović, D. Schöllhammer, and J. Steidl, Higherorder meshing of implicit geometries—Part I: Integration and interpolation in cut elements, Comput. Method. Appl. Mech. Eng., vol. 313, pp. 759-784, 2017. DOI: 10.1016/j.cma. 2016.10.019.
- T. Hoang, C. V. Verhoosel, F. Auricchio, E. H. van Brummelen, and A. Reali, Mixed isogeometric finite cell methods for the stokes problem, Comput. Method. Appl. Mech. Eng., vol. 316, pp. 400-423, 2017. DOI: 10.1016/j.cma.2016.07.027.
- S. Zhao, and G. W. Wei, Matched interface and boundary (MIB) for the implementation of boundary conditions in highorder central finite differences, Int J Numer Methods Eng., vol. 77, no. 12, pp. 1690-1730, 2009. DOI: 10.1002/nme.2473.
- S. May, and M. Berger, An explicit implicit scheme for cut cells in embedded boundary meshes, J Sci Comput., vol. 71, no. 3, pp. 919-943, 2017. DOI: 10.1007/s10915-016-0326-2.
- Heinz-Otto Kreiss, and N. Anders Petersson, An embedded boundary method for the wave equation with discontinuous coefficients, SIAM J. Sci. Comput., vol. 28, no. 6, pp. 2054-2074, 2006. DOI: 10.1137/050641399.
- H.-O. Kreiss, and N. A. Petersson, A second order accurate embedded boundary method for the wave equation with dirichlet data, SIAM J. Sci. Comput., vol. 27, no. 4, pp. 1141-1167, 2006. DOI: 10.1137/040604728.
- [21] H.-O. Kreiss, N. A. Petersson, and J. Ystrom, Difference approximations of the neumann problem for the second order wave equation, SIAM J. Numer. Anal., vol. 42, no. 3, pp. 1292-1323, 2004. DOI: 10.1137/S003614290342827X.
- [22] Z. Jomaa, and C. Macaskill, The shortley-weller embedded finite-difference method for the 3d poisson equation with mixed boundary conditions, J Comput Phys., vol. 229, no. 10, pp. 3675-3690, 2010. DOI: 10.1016/j.jcp.2010.01.021.
- [23] Z. Jomaa, and C. Macaskill, The embedded finite difference method for the poisson equation in a domain with an irregular boundary and dirichlet boundary conditions, J Comput Phys., vol. 202, no. 2, pp. 488-506, 2005. DOI: 10.1016/j.jcp.2004.07.011.
- J. L. Hellrung, Jr., L. Wang, E. Sifakis, and J. M. Teran, A second order virtual node method for elliptic problems with interfaces and irregular domains in three dimensions, J Comput Phys., vol. 231, no. 4, pp. 2015-2048, 2012. DOI: 10.1016/j.jcp. 2011.11.023.
- [25] L. Chen, H. Wei, and M. Wen, An interface-fitted mesh generator and virtual element methods for elliptic interface problems, J Comput Phys., vol. 334, pp. 327-348, 2017. DOI: 10.1016/j. jcp.2017.01.004.
- [26] J. Bedrossian, J. H. von Brecht, S. Zhu, E. Sifakis, and J. M. Teran, A second order virtual node method for elliptic problems with interfaces and irregular domains, J Comput Phys., vol. 229, no. 18, pp. 6405-6426, 2010. DOI: 10.1016/j.jcp.2010. 05.002.
- D. C. Assêncio, and J. M. Teran, A second order virtual node [27] algorithm for stokes flow problems with interfacial forces, discontinuous material properties and irregular domains, I Comput Phys., vol. 250, pp. 77-105, 2013. DOI: 10.1016/j.jcp. 2013.04.041.
- K. Mattsson, and M. Almquist, A high-order accurate [28] embedded boundary method for first order hyperbolic equations, J Comput Phys., vol. 334, pp. 255-279, 2017. DOI: 10. 1016/j.jcp.2016.12.034.

- P. Schwartz, M. Barad, P. Colella, and T. Ligocki, A cartesian grid embedded boundary method for the heat equation and Poisson's equation in three dimensions, J Comput Phys., vol. 211, no. 2, pp. 531-550, 2006. DOI: 10.1016/j.jcp.2005.06.010.
- G. Dakin, B. Despres, and S. Jaouen, Inverse lax-wendroff boundary treatment for compressible lagrange-remap hydrodynamics on cartesian grids, J Comput Phys., vol. 353, pp. 228-257, 2018. DOI: 10.1016/j.jcp.2017.10.014.
- P. Colella, D. T. Graves, B. J. Keen, and D. Modiano, A cartesian grid embedded boundary method for hyperbolic conservation laws, J Comput Phys., vol. 211, no. 1, pp. 347-366, 2006. DOI: 10.1016/j.jcp.2005.05.026.
- R. Crockett, P. Colella, and D. Graves, A cartesian grid embedded boundary method for solving the poisson and heat equations with discontinuous coefficients in three dimensions, J Comput Phys., vol. 230, no. 7, pp. 2451-2469, 2011. DOI: 10. 1016/j.jcp.2010.12.017.
- P. McCorquodale, P. Colella, and H. Johansen, A cartesian grid embedded boundary method for the heat equation on irregular domains, J Comput Phys., vol. 173, no. 2, pp. 620-635, 2001. DOI: 10.1006/jcph.2001.6900.
- H. Johansen, and P. Colella, A cartesian grid embedded bound-[34] ary method for Poisson's equation on irregular domains, J Comput Phys., vol. 147, no. 1, pp. 60-85, 1998. DOI: 10.1006/ jcph.1998.5965.
- J. B. Angel, J. W. Banks, and W. D. Henshaw, High-order upwind schemes for the wave equation on overlapping grids: Maxwell's equations in second-order form, J Comput Phys., vol. 352, pp. 534-567, 2018. DOI: 10.1016/j.jcp.2017.09.037.
- H. Uddin, R. Kramer, and C. Pantano, A cartesian-based embedded geometry technique with adaptive high-order finite differences for compressible flow around complex geometries, J Comput Phys., vol. 262, pp. 379-407, 2014. DOI: 10.1016/j.jcp. 2014.01.004.
- T. Song, A. Main, G. Scovazzi, and M. Ricchiuto, The shifted boundary method for hyperbolic systems: Embedded domain computations of linear waves and shallow water flows, J Comput Phys., vol. 369, pp. 45-79, 2018. DOI: 10.1016/j.jcp. 2018.04.052.
- [38] S. Hosseinverdi, and H. F. Fasel, An efficient, high-order method for solving poisson equation for immersed boundaries: Combination of compact difference and multiscale multigrid methods, J Comput Phys., vol. 374, pp. 912-940, 2018. DOI: 10.1016/j.jcp.2018.08.006.
- B. Wang, K. Xia, and G.-W. Wei, Second order method for solving 3d elasticity equations with complex interfaces, J Comput Phys., vol. 294, pp. 405-438, 2015. DOI: 10.1016/j.jcp. 2015.03.053.
- R. Guo, T. Lin, and Y. Lin, Approximation capabilities of immersed finite element spaces for elasticity interface problems, Numer. Methods Partial Differential Eq., vol. 35, no. 3, pp. 1243-1268, 2019. DOI: 10.1002/num.22348.
- T.-H. Huang, J.-S. Chen, M. R. Tupek, F. N. Beckwith, J. J. Koester, and H. E. Fang, A variational multiscale immersed meshfree method for heterogeneous materials, Comput Mech., vol. 67, no. 4, pp. 1059-1097, 2021. DOI: 10.1007/s00466-020-01968-1.
- A. Idesman, A new numerical approach to the solution of PDEs with optimal accuracy on irregular domains and Cartesian meshes. Part 1: the derivations for the wave, heat and Poisson equations in the 1-D and 2-D cases, Arch Appl Mech., vol. 90, no. 12, pp. 2621–2648, 2020. DOI: 10.1007/s00419-020-01744-w.
- B. Dey, and A. Idesman, A new numerical approach to the solution of PDEs with optimal accuracy on irregular domains and Cartesian meshes. Part 2: numerical simulation and comparison with FEM, Arch Appl Mech., vol. 90, no. 12, pp. 2649-2674, 2020. DOI: 10.1007/s00419-020-01742-y.
- A. Idesman, and B. Dey, A new 3-D numerical approach to the solution of PDEs with optimal accuracy on irregular domains and Cartesian meshes, Comput. Method. Appl. Mech. Eng., vol. 354, pp. 568-592, 2019. DOI: 10.1016/j.cma.2019.05.049.



- [45] A. Idesman, and B. Dey, Compact high-order stencils with optimal accuracy for numerical solutions of 2-d time-independent elasticity equations, Comput. Method. Appl. Mech. Eng., vol. 360, pp. 112699, 2020. DOI: 10.1016/j.cma.2019.112699.
- A. Idesman, and B. Dey, Accurate numerical solutions of 2-d elastodynamics problems using compact high-order stencils, Comput. Struct., vol. 229, pp. 106160, 2020. DOI: 10.1016/j. compstruc.2019.106160.
- [47] A. Idesman, and B. Dey, A new numerical approach to the solution of the 2-D Helmholtz equation with optimal accuracy on irregular domains and Cartesian meshes, Comput Mech., vol. 65, no. 4, pp. 1189-1204, 2020. DOI: 10.1007/s00466-020-01814-4.
- [48] A. Idesman, and B. Dey, New 25-point stencils with optimal accuracy for 2-d heat transfer problems. Comparison with the quadratic isogeometric elements, J Comput Phys., vol. 418, pp. 109640, 2020. DOI: 10.1016/j.jcp.2020.109640.
- A. Idesman, and M. Mobin, Optimal local truncation error method for solution of 3-D Poisson equation with irregular interfaces and unfitted Cartesian meshes as well as for postprocessing, Adv. Eng. Softw., vol. 167, pp. 103103, 2022. DOI: 10.1016/j.advengsoft.2022.103103.
- [50] A. Idesman, and B. Dey, Optimal local truncation error method to solution of 2-D time-independent elasticity problems with optimal accuracy on irregular domains and unfitted Cartesian meshes, Numer Meth Eng., vol. 123, no. 11, pp. 2610-2630, 2022. DOI: 10.1002/nme.6952.

- A. Idesman, and B. Dey, Optimal local truncation error method for solution of wave and heat equations for heterogeneous materials with irregular interfaces and unfitted cartesian meshes, Comput. Method. Appl. Mech. Eng., vol. 384, pp. 113998, 2021. DOI: 10.1016/j.cma.2021.113998.
- O. C. Zienkiewicz, and J. Z. Zhu, The superconvergent patch recovery and a posteriori error estimates. part 1: The recovery technique, Int. J. Numer. Meth. Eng., vol. 33, no. 7, pp. 1331-1364, 1992. DOI: 10.1002/nme.1620330702.
- [53] O. C. Zienkiewicz, and J. Z. Zhu, The superconvergent patch recovery and a posteriori error estimates, part 2: Error estimates and adaptivity, Int. J. Numer. Meth. Eng., vol. 33, no. 7, pp. 1365-1382, 1992. DOI: 10.1002/nme.1620330703.
- M. Kumar, T. Kvamsdal, and K. A. Johannessen, Superconvergent patch recovery and a posteriori error estimation technique in adaptive isogeometric analysis, Comput. Method. Appl. Mech. Eng., vol. 316, pp. 1086-1156, 2017. special Issue on Isogeometric Analysis: Progress and Challenges. DOI: 10.1016/j.cma.2016.11.014.
- A. Idesman, and B. Dey, The treatment of the Neumann boundary conditions for a new numerical approach to the solution of PDEs with optimal accuracy on irregular domains and Cartesian meshes, Comput. Method. Appl. Mech. Eng., vol. 365, pp. 112985, 2020. DOI: 10.1016/j.cma.2020.112985.
- K. J. Bathe, Finite Element Procedures, Upper Saddle River, NJ: Prentice-Hall Inc., 1996.
- H. P. Langtangen, and S. Linge, Finite Difference Computing with PDEs, Springer: Berlin, 2017.

Appendix A. The coefficients $b_{i,i}$ used in Eq. (24) for the 9-point stencils

The first 15 coefficients $b_{j,i}$ (i = 1, 2, ..., 15) are presented below. Please also see Appendix B and the attached file "b-coef.nb." For simplicity of notations, below we omit the first index j in $b_{j,i}$, $k_{j,p}$, $\bar{k}_{j,p}$, $m_{j,p}$, $\bar{m}_{j,p}$ related to the stencil number j=1, 2.

$$\begin{split} b_1 &= \sum_{p=1}^{N} k_p a_p + \sum_{m=1}^{N_G} q_{1,m} \\ b_2 &= \sum_{p=1}^{9} \left[k_p - k_p a_p \right] - \sum_{m=1}^{N_G} q_{1,m} \\ b_3 &= \sum_{p=1}^{9} \left[\bar{k}_p - \bar{k}_p a_p \right] - \sum_{m=1}^{N_G} q_{2,m} \\ b_4 &= \sum_{p=1}^{9} \left[\bar{k}_p - \bar{k}_p a_p \right] - \sum_{m=1}^{N_G} q_{2,m} \\ b_5 &= \sum_{p=1}^{9} k_p a_p r_{x,p} + \sum_{m=1}^{N_G} \left[d_{x,m} q_{1,m} + \lambda_* n_{x,m} q_{3,m} + 2\mu_* n_{x,m} q_{3,m} + \lambda_* n_{y,m} q_{4,m} \right] \\ b_6 &= \sum_{p=1}^{9} - k_p (-1 + a_p) r_{x,p} - \sum_{m=1}^{N_G} \left[d_{x,m} q_{1,m} - \lambda_{**} n_{x,m} q_{3,m} - 2\mu_{**} n_{x,m} q_{3,m} - \lambda_{**} n_{y,m} q_{4,m} \right] \\ b_7 &= \sum_{p=1}^{9} \bar{k}_p a_p r_{x,p} + \sum_{m=1}^{N_G} \left[d_{x,m} q_{2,m} + \mu_* n_{y,m} q_{3,m} + \mu_* n_{x,m} q_{4,m} \right] \\ b_8 &= \sum_{p=1}^{9} - \bar{k}_p (-1 + a_p) r_{x,p} - \sum_{m=1}^{N_G} \left[d_{x,m} q_{2,m} - \mu_{**} (n_{y,m} q_{3,m} + n_{x,m} q_{4,m}) \right] \\ b_9 &= \sum_{p=1}^{9} k_p a_p r_{y,p} + \sum_{m=1}^{N_G} \left[d_{y,m} q_{1,m} + \mu_* n_{y,m} q_{3,m} + \mu_* n_{x,m} q_{4,m} \right] \\ b_{10} &= -k_p (-1 + a_p) r_{y,p} - \sum_{m=1}^{N_G} \left[d_{y,m} q_{1,m} - \mu_{**} (n_{y,m} q_{3,m} + n_{x,m} q_{4,m}) \right] \\ b_{11} &= \sum_{p=1}^{9} \bar{k}_p a_p r_{y,p} + \sum_{m=1}^{N_G} \left[d_{y,m} q_{2,m} + \lambda_* n_{x,m} q_{3,m} + n_{x,m} q_{4,m} \right] \\ b_{12} &= - \sum_{p=1}^{9} \bar{k}_p (-1 + a_p) r_{y,p} - \sum_{m=1}^{N_G} \left[d_{y,m} q_{2,m} - \lambda_{**} n_{x,m} q_{3,m} - \lambda_{**} n_{y,m} q_{4,m} - 2\mu_{**} n_{y,m} q_{4,m} \right] \\ b_{13} &= \sum_{p=1}^{9} \left[(2\mu_* + \lambda_*) / \rho_* m_p a_p + 1 / 2k_p a_p r_{x,p}^2 \right] + \sum_{m=1}^{N_G} \left[(d_{x,m}^2 q_{1,m} + 4\mu_* d_{x,m} n_{x,m} q_{3,m} + 2\lambda_* (d_{x,m} (n_{x,m} q_{3,m} + n_{y,m} q_{4,m}))) / 2 \right] \end{aligned}$$

$$b_{14} = \sum_{p=1}^{9} \left[-m_p (2\mu_{**} + \lambda_{**})/\rho_{**} (-1 + a_p) + 1/2k_p (-1 + a_p) r_{x,p}^2 \right] + \sum_{m=1}^{N_G} 1/2 \left[d_{x,m} (d_{x,m} q_{1,m} + 4\mu_{**} n_{x,m} q_{3,m}) + 2\lambda_{**} d_{x,m} (n_{x,m} q_{3,m} + n_{y,m} q_{4,m}) \right] \\ b_{15} = \sum_{p=1}^{9} \left[(\bar{m}_p \mu_* a_p)/\rho_* + 1/2\bar{k}_p a_p r_{x,p}^2 \right] + \sum_{m=1}^{N_G} \left[1/2d_{x,m} (d_{x,m} q_{2,m} + 2\mu_* n_{y,m} q_{3,m} + 2\mu_* n_{x,m} q_{4,m}) \right]$$

Appendix B. The explicit form of Eq. (28) for the determination of the stencil coefficients

For simplicity of notations, below we omit the first index j in $b_{j,i}$, $k_{j,p}$, $\bar{k}_{j,p}$, $m_{j,p}$, $m_{j,p}$, $m_{j,p}$ related to the stencil number j=1, 2. The coefficients b_i in Eq. (24) can be represented as a linear function of the stencil coefficients m_p , \bar{m}_p , k_p , \bar{k}_p (p=1,2,...,9) and $q_{1,m}$, $q_{2,m}$, $q_{3,m}$, $q_{4,m}$ (m=1,2,...,5) as follows:

$$b_i = \sum_{j=1}^{36} s_{ij} \tilde{k}_j + \sum_{j=1}^{20} c_{ij} \tilde{q}_j, \qquad i = 1, 2, ..., 112,$$
(B.1)

where the coefficients s_{ij} and c_{ij} can be found from the expressions for the coefficients b_{ij} see A and the attached file "b-coef.nb." In Eq. (B.1) we use the following notations for the coefficients \tilde{k}_j and \tilde{q}_j :

$$\{\tilde{k}_1, \ \tilde{k}_2, \ ..., \tilde{k}_{36}\} = \{m_1, \ \bar{m}_1, \ k_1, \ \bar{k}_1, \ m_2, \ \bar{m}_2, \ k_2, \ \bar{k}_2, \ ..., \bar{k}_9\},$$
 (B.2)

$$\{\tilde{q}_1, \tilde{q}_2, ..., \tilde{q}_{20}\} = \{q_{1,1}, q_{2,1}, q_{3,1}, q_{4,1}, q_{1,2}, q_{2,2}, ..., q_{4,5}\}.$$
 (B.3)

Then using Eq. (B.1), the local system of linear algebraic equations for finding the stencil coefficients, Eq. (28), can be rewritten as follows:

$$\frac{\partial \bar{R}}{\partial \tilde{k}_{m}} = \sum_{l=1}^{24} \lambda_{l} \frac{\partial b_{l}}{\partial \tilde{k}_{m}} + 2 \left[\sum_{p=25}^{40} b_{p} \frac{\partial b_{p}}{\partial \tilde{k}_{m}} + h_{1} \sum_{p=41}^{60} b_{p} \frac{\partial b_{p}}{\partial \tilde{k}_{m}} + h_{2} \sum_{p=61}^{84} b_{p} \frac{\partial b_{p}}{\partial \tilde{k}_{m}} + h_{3} \sum_{p=85}^{112} b_{p} \frac{\partial b_{p}}{\partial \tilde{k}_{m}} \right]$$

$$= \sum_{l=1}^{24} \lambda_{l} s_{lm} + 2 \left[\sum_{j=1}^{36} \left(\sum_{p=25}^{40} s_{pj} s_{pm} + h_{1} \sum_{p=41}^{60} s_{pj} s_{pm} + h_{2} \sum_{p=61}^{84} s_{pj} s_{pm} + h_{3} \sum_{p=85}^{112} s_{pj} s_{pm} \right) \tilde{k}_{j} \right]$$

$$+ \sum_{j=1}^{40} \left(\sum_{p=25}^{40} c_{pj} s_{pm} + h_{1} \sum_{p=41}^{60} c_{pj} s_{pm} + h_{2} \sum_{p=61}^{84} c_{pj} s_{pm} + h_{3} \sum_{p=85}^{112} c_{pj} s_{pm} \right) \tilde{q}_{j} \right] = 0,$$

$$m = 1, 2, \dots, 36,$$
(B.4)

$$\frac{\partial \bar{R}}{\partial \bar{q}_{m}} = \sum_{l=1}^{24} \lambda_{l} \frac{\partial b_{l}}{\partial \tilde{q}_{m}} + 2 \left[\sum_{p=25}^{40} b_{p} \frac{\partial b_{p}}{\partial \tilde{q}_{m}} + h_{1} \sum_{p=41}^{60} b_{p} \frac{\partial b_{p}}{\partial \tilde{q}_{m}} + h_{2} \sum_{p=61}^{84} b_{p} \frac{\partial b_{p}}{\partial \tilde{q}_{m}} + h_{3} \sum_{p=85}^{112} b_{p} \frac{\partial b_{p}}{\partial \tilde{q}_{m}} \right]$$

$$= \sum_{l=1}^{24} \lambda_{l} c_{lm} + 2 \left[\sum_{j=1}^{36} \left(\sum_{p=25}^{40} s_{pj} c_{pm} + h_{1} \sum_{p=41}^{60} s_{pj} c_{pm} + h_{2} \sum_{p=61}^{84} s_{pj} c_{pm} + h_{3} \sum_{p=85}^{112} s_{pj} c_{pm} \right) \tilde{k}_{j} \right]$$

$$+ \sum_{j=1}^{40} \left(\sum_{p=25}^{40} c_{pj} c_{pm} + h_{1} \sum_{p=41}^{60} c_{pj} c_{pm}^{1} + h_{2} \sum_{p=61}^{84} c_{pj} c_{pm} + h_{3} \sum_{p=85}^{112} c_{pj} c_{pm} \right) \tilde{q}_{j} = 0,$$

$$m = 1, 2, \dots, 20.$$
(B.5)

$$\frac{\partial \bar{R}}{\partial \lambda_m} = b_m = \sum_{j=1}^{36} s_{mj} \tilde{k}_j + \sum_{j=1}^{20} c_{mj} \tilde{q}_j = 0, \qquad m = 1, 2, ..., 24,$$
(B.6)

where Eqs. (B.4)–(B.6) form a system of 80 linear algebraic equations for the determination of the stencil coefficients \tilde{k}_j (j=1,2,...,36), \tilde{q}_j (j=1,2,...,20) as well as 24 Lagrange multiplier λ_l (l=1,2,...,24).